1-1-2011

Controlling the Morphology and Optical Properties of Nanostructured Materials: From Inorganic Nanoparticles to Conjugated Polymers

Sang-Jae Park
University of Pennsylvania, sangjaepark@lbl.gov

Controlling the Morphology and Optical Properties of Nanostructured Materials: From Inorganic Nanoparticles to Conjugated Polymers

Abstract
Soft materials such as nanoparticles and polymers show properties that are highly dependent on the nanoscale morphology as well as compositions. Thus, the ability to control their nanoscale morphology is important for both fundamental understanding and

technological applications of nanomaterials. My thesis work concerned two distinct nanomaterials possessing strong structure-dependent optical properties: 1) silica-based multicomponent nanoparticles and 2) amphiphilic conjugated block copolymers. The

multicomponent colloidal nanoparticles were composed of a fluorescent core and a metal shell separated by a silica spacer, where the florescence intensity from the core was controlled by adjusting the spacer thickness by layer-by-layer synthesis. The

supramolecular assemblies of amphiphilic conjugated block copolymers exhibited highly tunable photoluminescence properties depending on their self-assembly structures. These studies demonstrated that the specific structures can be designed and synthesized to improve the material properties and that the optical properties can be controlled by the self-assembled structures in a predetermined way.

Degree Type
Dissertation

Degree Name
Doctor of Philosophy (PhD)

Graduate Group
Chemistry

First Advisor
So-Jung Park

Subject Categories
Chemistry

CONTROLLING THE MORPHOLOGY AND OPTICAL PROPERTIES OF NANO-STRUCTURED MATERIALS: FROM INORGANIC NANOPARTICLES TO CONJUGATED POLYMERS

Sang-Jae Park

A DISSERTATION

in

Chemistry

Presented to the Faculties of the University of Pennsylvania in Partial Fulfillment of the Requirements for the Degree of Doctor of Philosophy

2011

_____

Professor So-Jung Park
Supervisor of Dissertation

_____

Professor Gary A. Molander
Graduate Group Chair

Dissertation Committee:

Christopher B. Murray, Professor of Chemistry
Larry G. Sneddon, Professor of Chemistry
Bradford B. Wayland, Professor of Chemistry

ABSTRACT

CONTROLLING THE MORPHOLOGY AND OPTICAL PROPERTIES OF NANO-STRUCTURED MATERIALS: FROM INORGANIC NANOPARTICLES TO CONJUGATED POLYMERS

Author's Name: Sang-Jae Park

Supervisor's Name: Prof. So-Jung Park

Soft materials such as nanoparticles and polymers show properties that are highly dependent on the nanoscale morphology as well as compositions. Thus, the ability to control their nanoscale morphology is important for both fundamental understanding and technological applications of nanomaterials. My thesis work concerned two distinct nanomaterials possessing strong structure-dependent optical properties: 1) silica-based multicomponent nanoparticles and 2) amphiphilic conjugated block copolymers. The multicomponent colloidal nanoparticles were composed of a fluorescent core and a metal shell separated by a silica spacer, where the florescence intensity from the core was controlled by adjusting the spacer thickness by layer-by-layer synthesis. The supramolecular assemblies of amphiphilic conjugated block copolymers exhibited highly tunable photoluminescence properties depending on their self-assembly structures. These

studies demonstrated that the specific structures can be designed and synthesized to improve the material properties and that the optical properties can be controlled by the self-assembled structures in a predetermined way.

Table of Contents

List of Schemes

List of Tables

List of Figures

Overview

The optical properties of soft-materials such as nanoparticles and polymers highly depend on their nanoscale morphology and thus elucidating the relationship is very important for fabricating the novel optical and electronic devices. For example, conjugated polymers have emerged as an important class of materials for a range of optoelectronic devices. Currently, one of the most important issues in this field is to learn how to control the polymer morphologies for the fundamental studies as well as the technological applications because their optical and electrical properties depend highly on the packing structures. The necessity for the nanoscale structure control is most easily shown in optimization of organic photovoltaics and light emitting devices. Their performance highly relies on controlling the nanoscale morphology of two semiconducting materials with different energy level to maximize charge separation, recombination, and transfer.

Furthermore, interest in nanoscale materials stems from the fact that the material properties change with their assembly structures as well as sizes. Individual anisotropic particles have interesting optoelectronic properties different from isotropic nanoparticles, which are caused by high-efficiency diffusion or scattering of light that can be useful in the development of novel optical devices. Additionally hybrid or multifunctional nanoparticles constructed from more than one component have also been attracting increasing interest due to their additional functionalities. The interaction between the two

components of the hybrids highly depends on the nanoscale structures which are determined by anisotropy, location of two components, existence of other barriers between two active components, composition, and so on, which can result in an active enhancement or modulation of their optoelectronic properties.

In this thesis, I describe the relationship between materials properties and structures by using inorganic multicomponent nanoparticles and conjugated block copolymers. There are many ways to fabricate the specific structures. Of those, bottom-up approach is a very promising way to fabricate very complicated structures, which are being always used by the nature without human intervention. Supramolecular structures with controlled shapes, dimensions, and properties are of interest for multicomponent systems having defined function in devices for optics and electronics. This study demonstrates how the specific structures can be designed and synthesized to improve the materials properties and the optical properties can be controlled by the self-assembled structures in a predetermined way.

In Part I, I describe the synthesis of the multicomponent nanoparticles composed of fluorescent nanoparticles and metal nanostructures. In Part II, the spontaneous shape evolution of silica nanoparticles into hollow structures is described. In Part III, the synthesis and optical studies of a conjugated block copolymer are described. In Part IV, it is shown that the as-synthesized conjugated block copolymers can be used as a good dispersant of single-wall carbon nanotubes and a structure-directing template.

Part I:

Design and Synthesis of Multicomponent Nanomaterials Composed of Fluorescent Nanoparticles and Metal Nanostructures

2.1. Introduction

During the past decade, synthetic methods for making monodisperse nanostructures have been greatly improved for materials of various compositions.[1-3] This advancement enabled researchers to better understand the size- and shape-dependent properties emerging at the nanometer scale,[4] making their technological application a more realistic goal. An important direction in this research field today is to extend single component nanoparticles to multicomponent hybrid systems possessing well-defined subdomains composed of different types of materials.[5-8] The primary motivation behind this effort is to create multifunctional nanoparticles that combine the properties of individual components to eliminate the need for introducing a set of separate nanostructures for different tasks. Recently, substantial progress has been made towards synthesizing binary and ternary nanostructures composed of combinations of metal, magnetic, and semiconductor nanoparticles.[6-9] However, thus far, the focus in this area has been on developing new and more efficient synthetic methods to generate such hybrid species, rather than optimizing the structures to maximize the properties of each

component. Particularly, in most previously reported hybrid structures composed of semiconductor and metal subdomains,[8,9] light emitting properties of semiconductor particles were almost completely lost due to charge transfer or metal-induced fluorescence quenching[10-12] via Förster-type energy transfer. Indeed, it is well recognized that the properties of each composing element in multicomponent nanostructures are affected by the presence of other particles through the coupling between the individual components, and these interactions can be tuned by controlling their spatial organization. Therefore, the design and synthesis of hybrid systems with controllable geometrical relationships is crucial both in a fundamental understanding of the coupling and in their technological applications. This aspect is especially critical in composite systems involving fluorescent nanoparticles and metallic nanostructures, as the metal can drastically alter the optical properties of nearby fluorophores.[11]

Herein, the fabrication of multilayer nanoparticles featuring fluorescent nanoparticle cores, silica spacers, and gold shells with controllable geometries and optical properties is described (Scheme 1). Specifically, tetramethylrhodamine isothiocyanate (TRITC) doped silica nanoparticles were used as fluorescent cores. The core particles were each enclosed in an additional layer of silica. Then, the double layer particles were subsequently coated with hemispherical gold metal shells. This structural motif allows for the precise adjustment over the average metal-fluorophore distance and thus the degree of fluorescence quenching by tuning the thickness of the silica spacer layer.

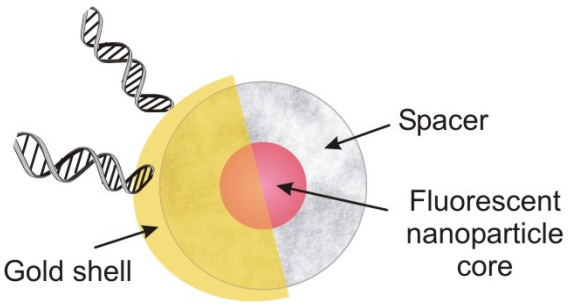

Scheme 1. Structure of multilayer particles composed of fluorescent core, silica spacer, and gold shell.

Based on this approach, the synthesis of composite materials of gold and fluorescent nanoparticles that retain the light emission properties of the core particles and the useful surface properties of gold is demonstrated. Furthermore, It is shown that these multilayer particles can be conjugated to DNA via well-established gold-thiol chemistry [13] and used in a DNA detection application.

2.2. Experimental Section

Materials. 3-Aminopropyltriethoxysilane (APS), tetraethyl orthosilicate (TEOS), ammonium hydroxide, 2-propanol, and 3-aminopropyltrimethoxysilane (APTMS) were purchased from Aldrich. Tetramethylrhodamine isothiocyanate (TRITC) and FluoSpheres® (amine-modified microspheres, 0.2 μm, red fluorescent (580/605), batch# 25925W) were purchased from Molecular Probes. Absolute ethanol was purchased from Pharmco. Ultrapure water (18 MΩ, Barnstard) was used exclusively for all reactions. Gold (splatters, 99.99% pure) metal was purchased from Cerac. All starting materials and solvents were used as received without further purification.

Instrumentation. Transmission electron microscopy (TEM) was performed on a JEOL TEM-2010 operating at 200 kV accelerating voltage to determine particle size distribution. Fluorescence emission measurements were recorded with a Fluorolog®-3 spectrofluorometer (HORIBA Jobin Yvon, Inc.) utilizing an R928 PMT detector. To deposit a noble metal thin film onto silica nanoparticles, an AUTO 306 Vacuum Coater with turbomolecular pumping system (BOC Edwards) was used.

Synthesis of TRITC-doped Silica Nanoparticles (TRITC-SiO_2). In order to synthesize TRITC-SiO_2 nanoparticles, a TRITC-labeled silica precursor (TRITC-APS) was first prepared.[14] Typically, TRITC (0.2 mg, 0.45 μmol) dissolved in 2 mL of anhydrous ethanol was mixed with APS (5 μL, 21.37 μmol). Then, the solution was stirred gently for 12 h in the dark. For the preparation of TRITC-SiO_2 nanoparticles, TEOS (1.42 mL, 6.37 mmol), NH_4OH (28% NH_3 in water, 1.92 mL), and 1 mL of the ethanolic solution of TRITC-APS were added to 33.5 mL ethanol in a 100 mL reaction flask equipped with a stir bar; the reaction mixture was stirred at room temperature for 12 h. The synthesized TRITC-SiO_2 nanoparticles were precipitated with excess methanol (100 mL) and then purified by centrifugation (7500 rpm, 30 min) and redispersed in ethanol (25 mL) to remove free TRITC. This purification process was repeated several times. Finally, purified particles were stored in 25 mL ethanol. The final concentration of nanoparticles was estimated to be 1.76×10^{13} particles/mL, assuming that the silica density[15] is 2.03 g/cm^3.

Synthesis of Silica-coated TRITC-SiO_2 particles (TRITC-SiO_2@SiO_2). To coat TRITC-SiO_2 particles with an additional layer of silica, an ethanolic solution of TRITC-SiO_2 particles (~ 1.76×10^{13} particles/mL, 2mL) and an aliquot of NH_4OH (0.960 mL for 26 nm-thick silica spacer or 1.152 mL for 36 nm-thick silica spacer) were added to 20 mL ethanol in a 50 mL reaction flask equipped with a stir bar. After 10 min stirring, TEOS (710 μL for 26 nm spacer or 852 μL for 36 nm spacer) was added to the mixture,

and the solution was stirred for 16 h. Prepared TRITC-SiO_2@SiO_2 nanoparticles were precipitated with excess ethanol (100 mL) and then purified by centrifugation (7500 rpm, 30 min) and redispersed in ethanol (25 mL). This purification process was repeated several times. Finally, purified particles were stored in 10 mL ethanol. The final concentration of nanoparticles was estimated to be 3.53×10^{12} particles/mL.

Amine-functionalization of TRITC-SiO_2 and TRITC-SiO_2@SiO_2 particles. In a typical experiment, 2 mL of ethanolic solution of nanoparticles (~ 1.76×10^{13} particles/mL for TRITC-SiO_2 or ~ 3.53×10^{12} particles/mL for TRITC-SiO_2@SiO_2 particles) were diluted to 20 mL with ethanol in a 100 mL reaction flask, and then APTMS (100 μL, 0.57 mmol) was added to the solution. The reaction mixture was stirred for 12 h at room temperature, after which the solution was stirred at 50 ^{o}C for one additional hour.[16] The amine-functionalized TRITC-SiO_2 and TRITC-SiO_2@SiO_2 nanoparticles were purified by centrifugation as described above. Purified particles were dispersed in 10 mL water.

Synthesis of Au coated TRITC-SiO_2@SiO_2 particles (TRITC-SiO_2@SiO_2@Au). The amine-functionalized nanoparticle solution (~ 7.1 x 10^{11} particles/mL, 200 μL) was dropped on a cleaned glass microscope slide. The glass slide was placed in a humidity chamber in the dark for ~1 h, after which it was gently washed with water and dried by a stream of nitrogen gas. A thin layer of gold (20 nm) was then deposited onto the glass surface using a thermal evaporator. The half-coated nanoparticles were released from the

glass slide by sonicating the slide in water (20 mL) for ~3 min. The released particles were stored in the dark.

Multilayer Particles with Commercial Fluorosphere Cores (FluoSpheres®@SiO_2@Au). Commercial FluoSpheres® (amine-modified polymer particles, 0.2 μm, red fluorescent (580/605)) purchased from Molecular Probes were first coated with a thin layer of silica by following a modified literature procedure.[17] Typically, 0.25 mL of commercial FluoSpheres® solution (~ 4×10^{12} particles/mL) was diluted to 2 mL with water in a 20 mL reaction flask. 2-propanol (10 mL), NH_4OH (28% NH_3 in water, 60 μL), and TEOS (109 μL, 0.490 mmol) were added to the solution and the mixture was stirred at room temperature for 4h. The synthesized FluoSpheres®@SiO_2 nanoparticles were precipitated with excess 2-propanol (100 mL) and then purified by centrifugation (7500 rpm, 30 min) and redispersed in 2-propanol (25 mL). This purification process was repeated several times. Finally, purified particles were stored in ethanol (25 mL) until further use. FluoSpheres®@SiO_2 nanoparticles were functionalized with amine and coated with gold by following the similar procedure described above except that the concentration of FluoSpheres®@SiO_2 nanoparticles used for amine functionalization was 5.0×10^{10} particles/mL and the concentration of amine-functionalized nanoparticles used for gold coating was ~ 4.0×10^{10} particles/mL.

Single Particle Fluorescence Measurements. To prepare samples for single particle fluorescence measurements, 200 μL of a suitably concentrated (~5 x 10^{11} particles/mL)

solution of desired nanoparticles were placed onto a microscope glass slide. Slides were then allowed to rest in the dark in a humidity chamber (to prevent evaporation) for approximately 40 minutes, after which they were washed with water and dried by a stream of clean nitrogen gas. The glass slides used in this study were pre-cleaned by washing them with boiling methanol and then a hot cleaning solution[18] (NH_4OH : H_2O_2 : H_2O = 1 : 1 : 5 by volume). Gold layers were deposited onto the sample using a thermal evaporator as described above. In order to directly compare gold coated particles to those with no coating, only half of any given slide was coated with gold.

Single-particle photoluminescence (PL) intensities and spectra were acquired utilizing a home-built single-molecule imaging system. Briefly, the 514.5 nm laser line emanating from an Argon ion laser (Melles Griot IMA 101040ALS) was isolated using an equilateral prism and expanded using a 10x beam expander. The expanded beam was directed into the entrance aperture of an Olympus IX71 Microscope after passing through neutral density and interference filters, as well as polarization optics (thin film polarizer, multiorder quarter wave plate). Inside the microscope, the excitation source was reflected by a dichroic beamsplitter (Chroma, z514rdc) into a high magnification microscope oil immersion objective (100X, NA =1.4), and focused onto the sample. Adjustment of the sample x- and y-position was effected by a piezoelectric scanner (Picoquant, PI-P-733.2CL). Fluorescent light emitted from the sample was collected using the same microscope objective and passed out of the microscope through

a side port. Residual excitation light was filtered using a high precision notch filter (CVI Laser Optics, RNF-514.5) and the PL light was directed into one of two detectors: (1) for fluorescence imaging, an avalanche photodiode (APD) photon counting module (Perkin Elmer, SPCM-AQR-14) and (2) for fluorescence spectra, a spectrometer (Princeton Instruments/Acton, SP2156) and CCD camera (Princeton Instruments, PhotonMAX 512B). Data was collected and analyzed using commercial software (PicoQuant Sym-Pho-Time for PL intensities and fluorescence trajectories and WinSpec32 for PL spectral data).

DNA-Functionalization of Multilayer Particles. Oligonucleotides used in this study were purchased from IDT. 5'-alkanethiol modified oligonucleotides (5'-HS-DNA: 5' HS-AAA AAA AAA AAT CCT TAT CAA TAT T 3') were immobilized on the gold surface of FluoSphere®@SiO_2@Au particles. For this experiment, FluoSphere®@SiO_2 particles were coated with gold by a slightly modified procedure from that described above. First, glass slides were functionalized with APTMS to render an amine-modified substrate to promote the binding of slightly negatively charged FluoSphere®@SiO_2 particles onto the glass slide. Typically, glass slides cleaned with piranha solution were placed in aq. solution of APTMS (1 % (v/v)) and acetic acid (1 mM) for 30 min. The glass slides were rinsed with water and cured at 120 ^{o}C in vacuum.[19] Then, an aq. solution of FluoSphere®@SiO_2 (4.0×10^{10} particles/mL, 100 μL) was placed onto the amine-functionalized glass slide. After 12 hrs, the glass slide was rinsed with water and

gently dried with a stream of nitrogen gas. Subsequently, thin layers of titanium (5 nm) and gold (20 nm) were deposited onto the glass slide by a thermal evaporator. The gold surface was functionalized with 5' HS-DNA by placing 100 µL of 1 M NaCl, 100 mM phosphate buffer solution (pH 7) of 5' HS-DNA (1.0 µM) onto the glass slide. After 12 hrs, the glass slides were rinsed with water and sonicated to release the FluoSphere®@SiO_2@Au particles. The DNA-modified particles were purified by the centrifugation at 7,000 rpm, and redispersed in water (0.1 mL). The particles were stored in a refrigerator (4 ^oC) until further use.

To evaluate the complementary sequence recognition of DNA-modified multilayer particles, capture DNA strands (3' HS-DNA: 3' HS-AAA AAA AAA ACT CCC TAA TAA CAA T 5') were immobilized on a thin film of gold by placing 1 M NaCl, 100 mM phosphate buffer solution of 3' HS-DNA (1.0 µM, 100 µL) onto the gold substrate. After incubating 12 hrs, the glass slide was rinsed with water. The gold substrate was prepared by thermally evaporating thin layers of titanium (5 nm) and gold (20 nm) onto a cleaned glass slide.

To test the complementary binding of DNA, an aq. solution of target DNA (5' GAG GGA TTA TTG TTA AAT ATT GAT AAG GAT 3') (10 µL, 10 µM) was mixed with 100 µL of the DNA-modified FluoSphere®@SiO_2@Au. The salt concentration and the pH of the solution were adjusted to 0.2 M NaCl and 10 mM phosphate buffer (pH 7). After 4 hrs, the solution was centrifuged at 7,000 rpm and the precipitates were

redispersed in 143 μL of phosphate buffered saline solution (PBS) (0.2 M NaCl, 10 mM phosphate, pH 7). The mixture of target DNA and DNA-modified multilayer particles was placed onto the DNA-modified gold surface. After incubating 12 hours, the glass slide was rinsed with a PBS buffer solution (0.2 M NaCl, 10 mM phosphate, pH 7) and 0.3 M ammonium acetate solution, dried with a stream of clean nitrogen gas, and imaged by a fluorescence microscope. For a control experiment, DNA-modified FluoSphere®@SiO_2@Au was applied to a 3' HS-DNA modified gold substrate without the target DNA while keeping other conditions identical.

2.3. Synthesis of TRITC-SiO_2@SiO_2@Au

As the first step towards the synthesis of gold coated fluorescent nanoparticles, fluorophore-labeled silica nanoparticles (TRITC-SiO_2) were synthesized by covalently incorporating TRITC into a silica matrix by hydrolyzing and co-condensing TRITC-functionalized silica precursors (APS-TRITC) and TEOS (Scheme 2). Covalently linked fluorophore molecules are less prone to leaking out from the silica matrix than fluorophores incorporated into silica particles by other methods.[20] The diameter of fluorophore-labeled silica particles (TRITC-SiO_2) was determined to be 80 ± 2 nm by TEM (Figure 1A, B). A single TRITC-SiO_2 nanoparticle was estimated to contain, on average, ~550 TRITC molecules.

Additional silica was deposited onto the TRITC-SiO_2 core particles as a spacer

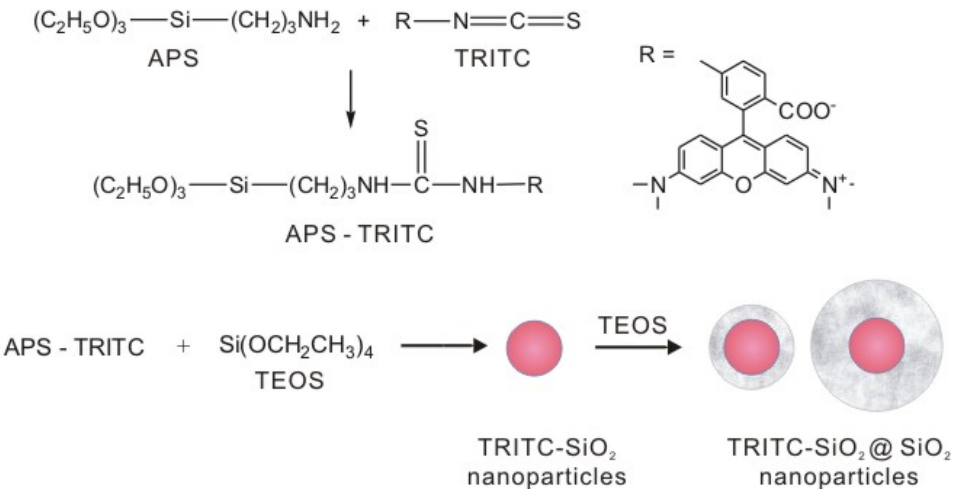

Scheme 2. Synthesis of TRITC-SiO_2 and TRITC-SiO_2@SiO_2 nanoparticles

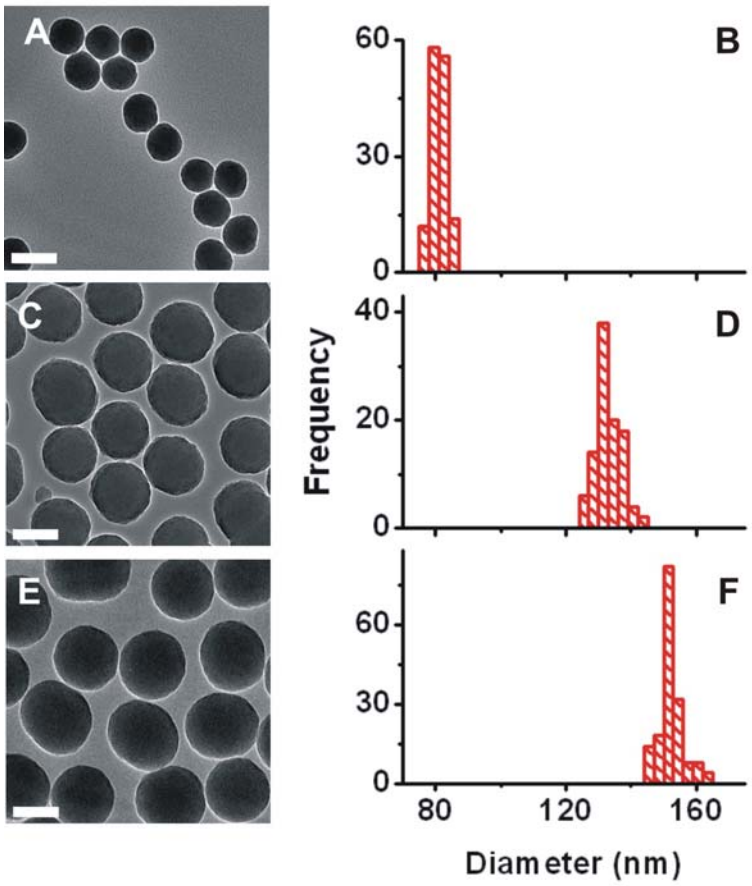

Figure 1. TEM images and size distribution histograms of TRITC-SiO_2 and TRITC-SiO_2@SiO_2 nanoparticles: (A) and (B) TRITC-SiO_2; (C) and (D) TRITC-SiO_2@SiO_2 with shell thickness of 26 nm; (E) and (F) TRITC-SiO_2@SiO_2 with shell thickness of 36 nm. Scale bar: 100 nm

layer between the fluorescent nanoparticles (TRITC-SiO_2) and gold shell in order to study the effect of the spacer thickness on the interactions between these two subdomains. A uniform silica spacer layer was grown onto the TRITC-SiO_2 core particles by hydrolyzing and condensing TEOS in the presence of the fluorophore-labeled silica particles. The thickness of the spacer layer was controlled by adjusting the amount of TEOS and ammonium hydroxide. TEM images and size distribution histograms of silica coated TRITC-SiO_2 particles (TRITC-SiO_2@SiO_2) with two different silica spacer thicknesses are presented in Figure 1. The silica spacer thicknesses of those particles were determined to be 26 nm ± 4 nm and 36 nm ± 5 nm respectively from the diameters of the particles (132 ± 4 nm and 152 ± 4 nm respectively) (Figure 1D and 1F). The two silica spacer thicknesses (26 nm and 36 nm) were chosen because they are expected to sufficiently separate the fluorescent core and metal shell to prevent the metal-induced quenching, and potentially allow for the metal-induced enhancement.[21,22] The core-shell structure of TRITC-SiO_2@SiO_2 particles was clearly demonstrated by an etching experiment, where different degrees of etching in core and shell regions resulted in clearly visible subdomains of core-shell structure (Figure 2). This result also indicates that the silica coating was uniform throughout the sample and the nucleation of new particles was rare during the silica coating.

The synthesized TRITC-SiO_2@SiO_2 nanoparticles were subsequently coated with gold metal on one side by the method described in Figure 3A. To accomplish this, the

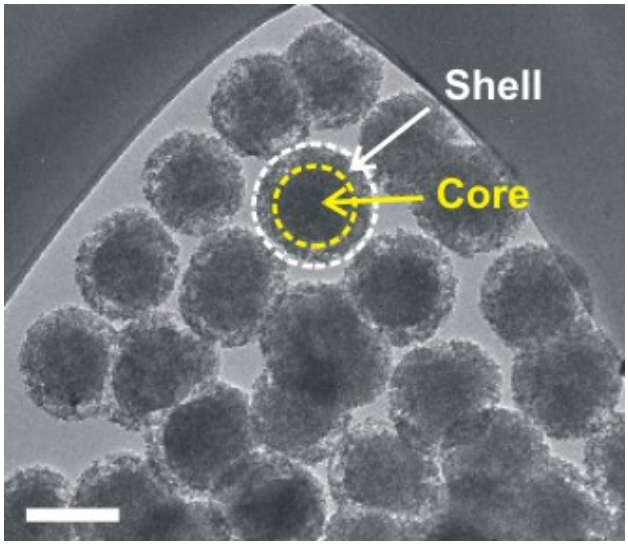

Figure 2. A TEM image of TRITC-SiO_2@SiO_2 nanoparticles treated with concentrated NaOH solution, revealing clearly visible core and shell structure. Scale bar: 100 nm.

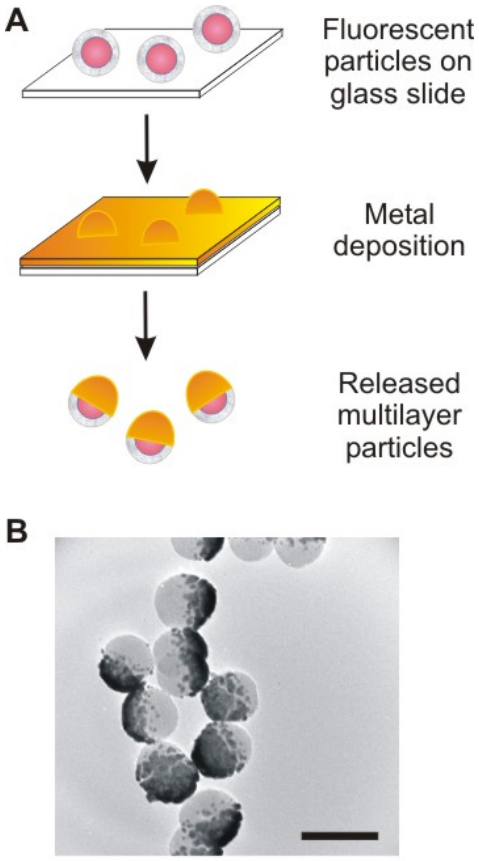

Figure 3. (A) Schematic description of the synthesis of TRITC-SiO_2@SiO_2@Au nanoparticles. (B) A TEM image of released TRITC-SiO_2@SiO_2@Au particles. Scale bar: 200 nm.

TRITC-SiO_2@SiO_2 nanoparticles were first functionalized with APTMS and deposited on a clean glass microscope slide. The amine-functionalization aids in adhering nanoparticles to the slightly negatively charged glass substrate. Then, a thin layer of gold (20 nm) was deposited onto the nanoparticles using a thermal evaporator to form TRITC-SiO_2@SiO_2@Au nanoparticles. The glass slides were then placed in water and TRITC-SiO_2@SiO_2@Au particles were released by sonication. Figure 3B shows a TEM image of the released TRITC-SiO_2@SiO_2@Au nanoparticles, illustrating that all released particles are coated on one hemisphere with a thin layer of gold metal. The asymmetric conformation of the hemispherical gold layer of these composite materials can reduce reabsorption of light emitted from the nanoparticle cores by the surrounding gold surface, a problem which could be encountered in particles coated completely by gold shells. Indeed, such species have been synthesized by using the seed-growth method.[16] The PL of those particles was in fact severely dampened by the surrounding gold, although it may be possible to generate light emitting particles that are completely covered by gold by judiciously choosing the combinations of fluorophore molecules and metal nanostructures and their arrangement. Furthermore, hemispherical gold coatings may ultimately provide an entryway into a whole host of new and interesting asymmetrically functionalized nanoarchitectures.

2.4. Single-Particle PL Measurements of TRITC-SiO_2@SiO_2@Au Nanoparticles

In order to assess the effect of the silica spacer on the photoluminescent capacity of gold-coated TRITC-labeled silica particles, the PL intensities of TRITC-SiO_2 and TRITC-SiO_2@SiO_2 (shell thickness = 26 nm or 36 nm) nanoparticles were recorded at the single particle level in the presence and absence of a thin gold coating. Single particle measurements allow for the direct comparison of the PL characteristics of the samples at each preparation step and ensure a reliable comparison between the particles with and without gold coating. In this study, examining the emission characteristics at the single-particle level was necessary because of the large variations in particle concentrations during the multistep synthesis and purification. Single-particle PL samples were prepared as depicted in Figure 3A, excluding the release step. The particle density was kept to ~10-20 per 10 μm by 10 μm area to ensure good isolation of individual particles. Figures 4A and 4C display representative PL images of gold-coated TRITC-SiO_2 and TRITC-SiO_2@SiO_2 nanoparticles with a shell thickness of 26 nm collected at the same illumination and data collection conditions. Note that particles with no spacer layer are barely visible in the image because of the metal induced quenching at short distances. This measurement clearly shows that the silica spacer effectively attenuates the quenching of TRITC fluorescence by the gold shell due to the larger mean physical separation between the gold shell and the TRITC fluorophores that are dispersed throughout the TRITC-SiO_2 core. The same PL images of gold-coated TRITC-SiO_2

nanoparticles are presented with a lower intensity (Z) scale in Figure 5, to show that the TRITC-SiO_2 sample has in fact the similar number of weakly emitting particles. The residual PL from the TRITC-SiO_2 particles can come from the TRITC molecules located towards the center of TRITC-SiO_2 core. PL intensity histograms constructed from the images (Figure 4B and 4D) indicate that the mean PL intensity for gold-coated TRITC-SiO_2@SiO_2 nanoparticles possessing 26 nm silica shells (Figure 4D) is substantially (~400 %) higher than that of gold-coated TRITC-SiO_2 nanoparticle cores without a spacer (Figure 4B). This result is better depicted by the plot of mean PL intensity versus the spacer thickness shown in Figure 4E. Particles with a thicker (36 nm) SiO_2 spacer exhibit an additional 100 % increase (compared to the core only particles) in their mean PL intensity (Figures 4E and F).

The synthesized particles were characterized at all stages by PL measurements at both ensemble and single particle levels. As shown in Figure 6, the addition of the silica shell did not appreciably alter the PL intensity distribution of the TRITC-SiO_2 core particles, confirming that the differences in the PL intensities with and without the spacer layer arise only from the changes in interactions with gold. This result is in contrast to the smaller particles (15 nm) reported by Wiesner and coworkers,[23] where a large increase of the PL intensity was observed with a silica coating. In our case, the local environment of the fluorophores is not significantly altered by the silica coating because most fluorophores are well imbedded in larger-sized silica particles even before

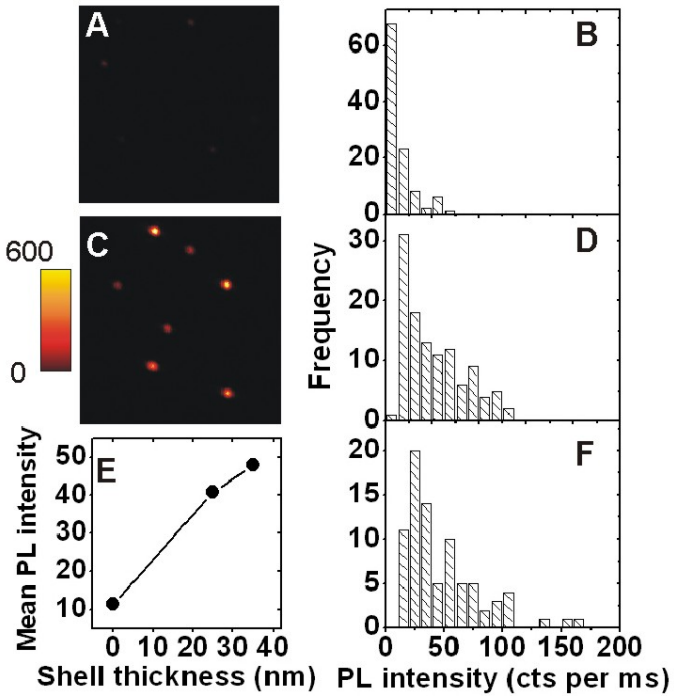

Figure 4. PL images and PL intensity histograms of individual gold-coated TRITC-SiO_2 core (A, B) and TRITC-SiO_2@SiO_2 nanoparticles with shell thicknesses of 26 nm (C, D) and 36 nm (F). The fluorescence images have dimensions of 10 μm x 10 μm; the scale bar represents the PL intensity in counts per 10 ms. Panel E shows a plot of the mean PL intensity as a function of silica layer thickness. An image identical to that shown in panel A, but with a reduced Z-axis (intensity) scale, is shown in Figure 5 for comparison. Experimental conditions: λ_{exc} = 514.5 nm, scan rate = 10 ms/pixel, resolution = 50 nm.

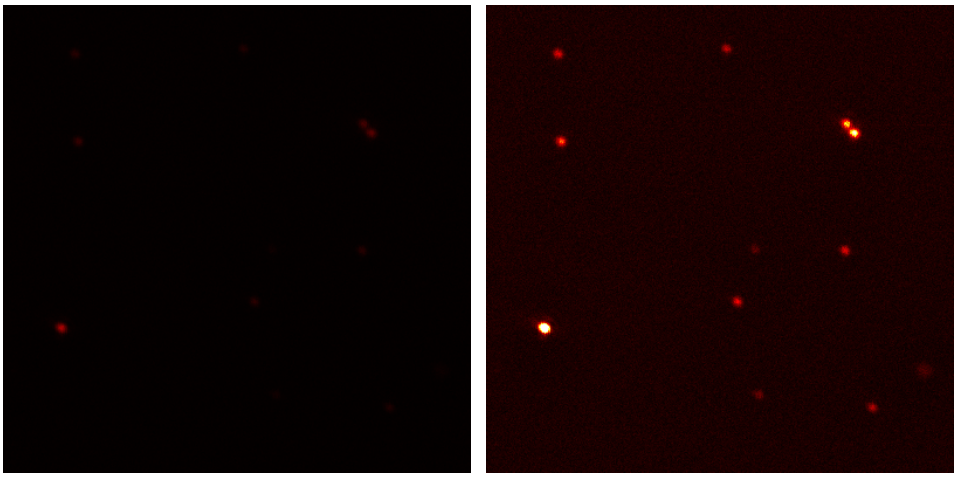

Figure 5. PL images of gold-coated TRITC-SiO_2 core particles plotted with two different intensity scales. *Left*: The same image presented in Figure 4 with the Z-axis (PL intensity) ranging from 0 to 600 counts. *Right*: An identical image with a Z-axis (PL intensity) ranging from 0 to 200 counts. This figure shows that weakly emitting gold-coated core particles are present in the image, which is difficult to see using the Z-axis that is used to present brighter gold-coated TRITC-SiO_2@SiO_2 core-shell particles in Figure 4. Experimental conditions: λ_{exc} = 514.5 nm, scan rate = 10 ms/pixel, resolution = 50 nm. Image dimensions: 20 x 20 microns.

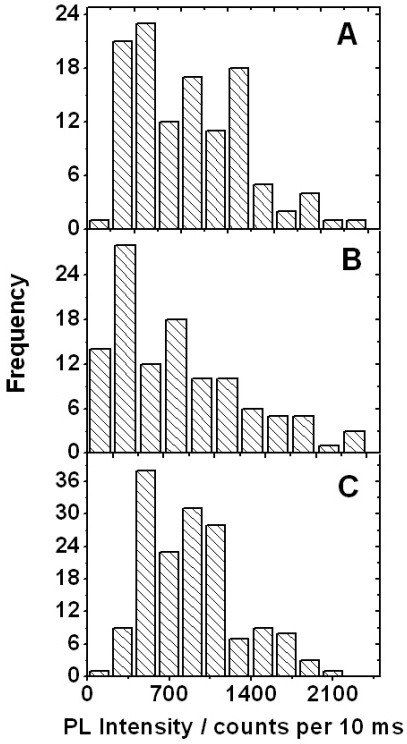

Figure 6. PL intensity histograms of individual gold-coated TRITC-SiO_2 core (A) and TRITC-SiO_2@SiO_2 nanoparticles with shell thicknesses of 26 nm (B) and 36 nm (C). The data were acquired for >100 individual particles in all cases. Experimental conditions: λ_{exc} = 514.5 nm, scan rate = 10 ms/pixel, resolution = 50 nm.

the coating. Emission wavelengths of the incorporated fluorophore molecules also remain similar before and after silica coating (Figure 7).

The experiment also revealed that, even when the SiO_2 spacer layer is 36 nm thick, the mean PL intensity of TRITC-SiO_2@SiO_2 particles was reduced by a factor of two upon gold coating. Such metal-fluorophore distance is expected to be too large for an efficient quenching interaction.[24] While more work needs to be done to understand the cause of the moderate PL quenching in particles with thick (26 ~ 36 nm) spacer layers, this effect may possibly be due to gold diffusion into the spacer layer during the coating process. Nonetheless, the improved PL intensity by adapting silica spacer layers led to dual functional particles that possess both brightly fluorescent cores and useful surface properties of gold. This effect should be more dramatic for fluorescent particles with a smaller diameter, where the core fluorescence can be completely quenched by gold without the spacer layer.

2.5. FluoSpheres®@SiO_2@Au Particles

To demonstrate the versatility of this strategy, the approach has been extended to commercial fluorescent nanoparticles (FluoSpheres®), which are 210 nm polymer particles labeled with fluorescent dye molecules. The polymer particles were encapsulated in silica shells following a modified literature procedure[17] to form FluoSpheres®@SiO_2 particles (Figure 8B). The silica shell thickness was determined to

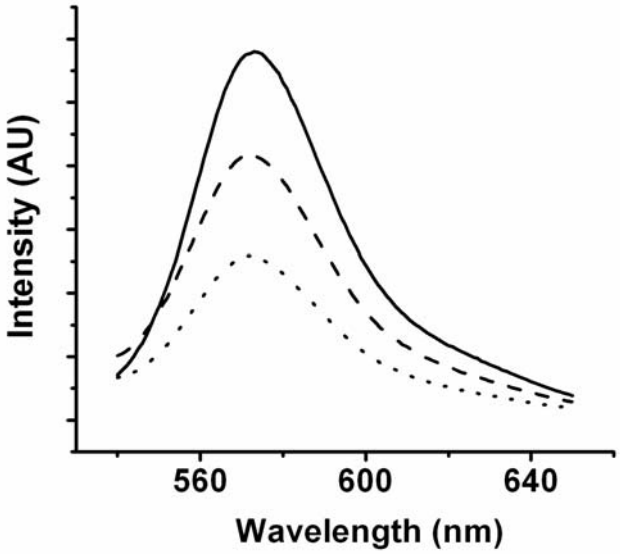

Figure 7. Ensemble PL spectra of TRITC-SiO_2 (solid line), TRITC-SiO_2@SiO_2 (dashed line, shell thickness = 26 nm), and TRITC-SiO_2@SiO_2 (dotted line, shell thickness = 36 nm) nanoparticles.

be 18 ± 5 nm. Subsequently, these silica coated commercial fluorescent nanoparticles were half-coated with gold (~30 nm) to form FluoSpheres®@SiO_2@Au (Figure 8C). Ensemble PL spectra of FluoSpheres® @ SiO_2 and released FluoSpheres®@SiO_2@Au particles were collected and plotted in Figure 8D.

2.6. Biofunctionalization of Multilayer Particles

The outer gold layer of the multilayer particles described here provides a convenient platform to immobilize biomolecules onto the particles via well-established gold-thiol chemistry without sacrificing the PL characteristics of core particles. To evaluate the potential of the multilayer particles for biological detection applications, we functionalized the gold surface of FluoSpheres®@SiO_2@Au particles with thiol-modified oligonucleotides (5' HS-DNA). In preparing gold-coated multilayer particles for DNA functionalization, the procedure for the gold coating step was slightly modified from that described above; here, an amine-functionalized glass coverslip was used to promote the sticking of FluoSpheres®@SiO_2 particles on the glass substrate, rather than amine-functionalizing the particles. This alternate strategy was adopted because it was found that the amine-functionalization of FluoSpheres®@SiO_2 particles used in the typical preparation can cause the aggregation of DNA-modified FluoSphere®@SiO_2@Au particles through electrostatic interactions between negatively charged DNA on gold and positively charged amine molecules on the other side of the particles. The DNA

functionalization was carried out by immobilizing thiol-modified oligonucleotides onto the gold film deposited on FluoSpheres®@SiO_2 particles. After the functionalization, DNA-modified FluoSpheres®@SiO_2@Au particles were released from the glass substrate via sonication. A thin layer of titanium was used as an adhesion layer for gold on the FluoSpheres®@SiO_2 particles. The prepared DNA-modified multilayer particles were evaluated in a DNA detection scheme described in Figure 9A. First, capture DNA strands (3' HS-DNA) were immobilized on a gold thin film, and the mixture of DNA modified multilayer particles and target DNA were applied to the DNA-modified gold substrate. A half of the target DNA is complementary to the DNA on multilayer particles and the other half is complementary to the capture DNA on the surface, bringing DNA-modified multilayer particles to the gold substrate. A control sample was prepared without the target DNA while keeping other conditions the same. The two samples were subsequently imaged by PL microscopy (Figure 9B and C). It is clearly seen that DNA-modified multilayer particles were bound to the DNA modified surface in the presence of target DNA while there was little bright PL spots visible in the control sample. This result demonstrates that the composite material described here can be readily functionalized by well-established biofunctionalization chemistry, while at the same time maintaining bright PL signatures necessary for a wide variety of biomedical applications.

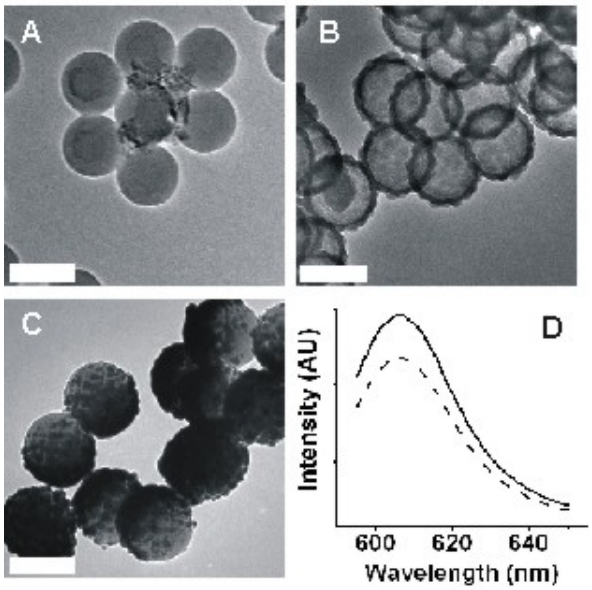

Figure 8. TEM images of (A) FluoSpheres®, (B) FluoSpheres®@SiO_2, and (C) FluoSpheres®@SiO_2@Au. (D) Ensemble PL spectrum of FluoSpheres®@SiO_2 (dashed line) and of FluoSpheres®@SiO_2@Au (solid line) in water.

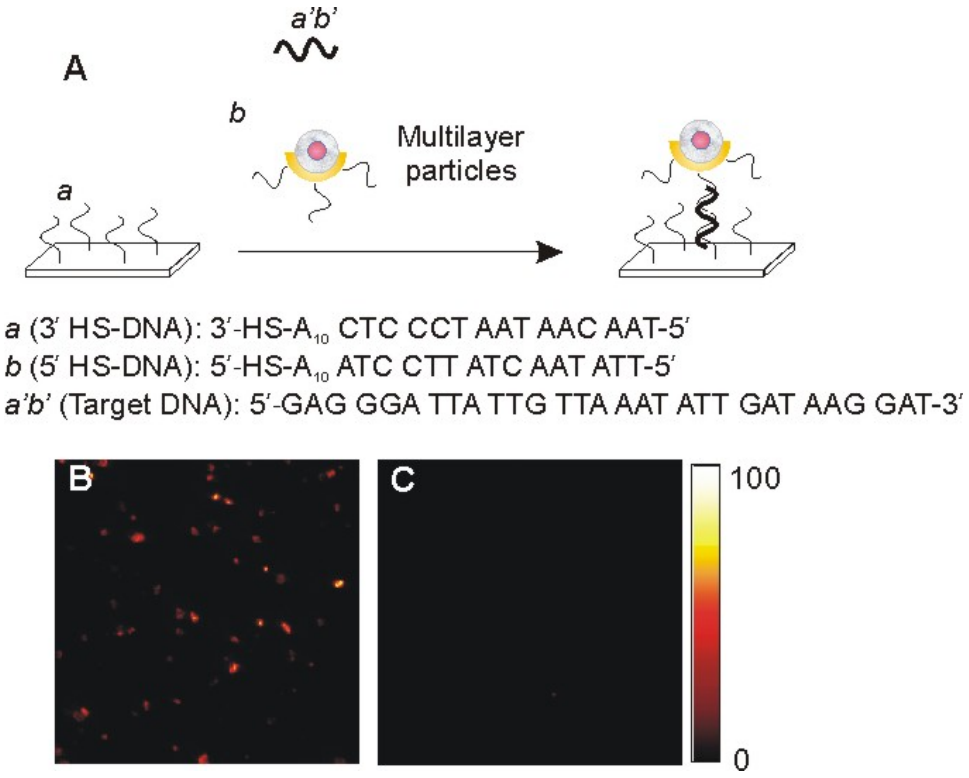

Figure 9. (A) Schematic description of complementary DNA recognition of multilayer particles. (B) A representative PL image of DNA-modified multilayer particles bound to DNA on a gold substrate via complementary target DNA. (C) A PL image of a control sample performed without the target DNA. Experimental details: scan rate = 2 ms per pixel, resolution = 80 nm, image dimensions = 40 μm x 40 μm.

2.7. Conclusion

There is a high demand in the field of nanomaterials for the fabrication of new composite species featuring multiple functional subdomains that are arranged in precisely defined geometries. In this study, we demonstrated the synthesis of novel composite nanomaterials composed of fluorophore-labeled silica cores and hemispherical gold overlayers that are separated by spectroscopically inert silica spacers. Single-particle PL measurements demonstrated that the silica spacer effectively reduces PL quenching of the core by the gold nanostructure.

The thickness of the spacer layer and the magnitude of this effect can be easily controlled by well-established sol-gel chemistry. It is important to note that the synthetic scheme is readily applicable to diverse types of fluorescent nanoparticles, including quantum dots. We have extended the strategy to commercial fluorophore-doped polymer nanoparticles to illustrate the versatility of this approach. As a proof-of-concept demonstration, we have functionalized the gold overlayer of multilayer particles with DNA using gold-thiol chemistry. The DNA-modified multilayer particles were used in a DNA detection application where the particles showed sequence-specific binding of DNA without evident nonspecific bindings. These results demonstrate the utility of the novel nanomaterials which simultaneously exhibit both bright PL and an available metal surface for biofunctionalization. Given the keen interest in fluorescent nanoparticles in a wide variety of biomedical applications, as well as useful surface properties of gold, we

anticipate that such hybrid structures are potentially useful in a broad range of applications which require highly emitting, biofunctionalized materials. It is also noteworthy that metal nanostructures can enhance fluorescence intensity and photostability of nearby fluorophores with the right combination of fluorescent molecules and metal nanostructures arranged in a proper geometry. An effort in this direction is currently underway.

2.8. Reference

(1) Park, J.; Joo, J.; Kwon, S. G.; Jang, Y.; Hyeon, T. *Angew. Chem. Int. Ed.* **2007**, *46*, 4630.

(2) Xia, Y.; Yang, P.; Sun, Y.; Wu, Y.; Mayers, B.; Gates, B.; Yin, Y.; Kim, F.; Yan, H. *Adv. Mater.* **2003**, *15*, 353.

(3) Jun, Y.-w.; Choi, J.-s.; Cheon, J. *Angew. Chem. Int. Ed.* **2006**, *45*, 3414.

(4) Burda, C.; Chen, X.; Narayanan, R.; El-Sayed, M. A. *Chem. Rev.* **2005**, *105*, 1025.

(5) Zeng, H.; Li, J.; Liu, J. P.; Wang, Z. L.; Sun, S. H. *Nature* **2002**, *420*, 395.

(6) Kim, H.; Achermann, M.; Balet, L. P.; Hollingthworth, J. A.; Klimov, V. I. *J. Am. Chem. Soc.* **2005**, *127*, 544.

(7) Li, Y.; Zhang, Q.; Nurmikko, A. V.; Sun, S. *Nano Lett.* **2005**, *5*, 1689.

(8) Shi, W.; Zeng, H.; Sahoo, Y. O., Ohulchanskyy, T. Y.; Ding, Y.; Wang, Z. L.; Swihart, M.; Prasad, P. N. *Nano Lett.* **2006**, *6*, 875.

(9) Mokari, T.; Rothenberg, E.; Popov, I.; Costi, R.; Banin, U. *Science* **2004**, *304*, 1787.

(10) Gueroui, Z.; Libchaber, A. *Phys. Rev. Lett.* **2004**, *93*, 166108.

(11) Lakowicz, J. R. *Anal. Biochem.* **2001**, *298*, 1.

(12) Dulkeith, E.; Morteani, A. C.; Niedereichholz, T.; Klar, T. A.; Feldmann, J.; Levi, S. A.; van Veggel, F. C. J. M.; Reinhoudt, D. N.; Moller, M.; Gittins, D. I. *Phys. Rev. Lett.* **2002**, *89*, 203002.

(13) Rosi, N. L.; Mirkin, C. A. *Chem. Rev.* **2005**, *105*, 1547.

(14) Imhof, A.; Megens, M.; Engelberts, J. J.; de Lang, D. T. N.; Sprik, R.; Vos, W. L. *J. Phys. Chem. B* **1999**, *103*, 1408.

(15) van Blaaderen, A.; Vrij, A. *J. Colloid Interface Sci.* **1993**, *156*, 1.

(16) Pham, T.; Jackson, J. B.; Halas, N. J.; Lee, T. R. *Langmuir* **2002**, *18*, 4915.

(17) Lu, Y.; McLellan, J.; Xia, Y. *Langmuir* **2004**, *20*, 3464.

(18) Min, H. S.; Joo, Y. C.; Song, O. S. *ASEM J. Electron. Packag.* **2004**, *126*, 120.

(19) Taton, T. A.; Lu, G.; Mirkin, C. A. *J. Am. Chem. Soc.* **2001**, *123*, 5164.

(20) Zhao, X.; Bagwe, R. P.; Tan, W. *Adv. Mater.* **2004**, *16*, 173.

(21) Enderlein, J. *Appl. Phys. Lett.* **2002**, *80*, 315.

(22) Anger, P.; Bharadwaj, P.; Novotny, L. *Phys. Rev. Lett.* **2006**, *96*, 113002.

(23) Ow, H.; Larson, D. R.; Srivastava, M.; Baird, B. A.; Webb, W. W.; Wiesner, U. *Nano Lett.* **2005**, *5*, 113.

(24) Lakowicz, J. R. *Principles of Fluorescence Spectroscopy*, 3rd ed.; Springer: New York, 2006, 841-859.

Part II:

Size-Dependent Shape Evolution of Silica Nanoparticles

3.1. Introduction

Silica nanostructures have been extensively studied for a wide range of applications including catalysts, drug delivery, and biological imaging.[1-3] The utility of silica particles in many applications relies on their inertness, just as glass is commonly used in our daily lives for the same reason. The ease of synthesis, well-established surface functionalization chemistry, and biocompatibility are also important merits of silica based nanomaterials.[4] However, the stability of nanometer-sized particles can be quite different from their bulk counterparts, and a trivial reactivity, which would not affect the bulk material, can cause a drastic change in the stability and the structural integrity of nanomaterials.

While the high surface energy and the instability arising at the nanometer scale could be problematic in many applications, it can be exploited to generate unique nanostructures. Here, it is demonstrated that hollow silica nanostructures can be spontaneously generated from solid silica particles without a template due to the high surface energy and reduced stability at the nanometer scale. Typically, hollow nanostructures are prepared by using soft or hard templates as sacrificial materials. For example, various mesoporous silica materials have been synthesized using small

surfactant molecules or block-copolymers as structure-directing and templating molecules.[5,6] Hollow silica nanoparticles and nanorods have been synthesized using various soft and hard templates such as polymers, metal, and semiconductor nanoparticles.[7-9] Only recently, there have been several reports on the templateless formation of hollow nanostructures. Xia and coworkers demonstrated the formation of Pd nanoboxes and nanocages based on the corrosion of Pd nanocubes and redeposition of Pd at the exterior of nanoboxes by the protecting layer of ethylene glycol.[10] Alivisatos and coworkers synthesized a series of hollow metal chalcogenide nanocrystals based on the Kirkendall effect.[11] Our study described herein provides a general route for the formation of hollow nanoparticles of porous materials. We show that different rules are applied for crystalline materials and amorphous materials in shape evolution by chemical reactions. The capability to further manipulate the morphology of porous nanoparticles will enable us to better control their local environment and properties. In addition, we show that the shape evolution of silica particles is size-dependent, demonstrating the importance of evaluating chemical stability and structural integrity as well as physical properties at different size ranges.

In this study, a series of silica nanoparticles of different sizes were synthesized by the well-established Stöber[12] and microemulsion methods[13], which are the two common methods for making silica particles. Both methods are based on the base catalyzed hydrolysis and condensation of tetraethylorthosilicates (TEOS). The main difference is

that the microemulsion method uses surfactants to disperse a small amount of water in an organic solvent. Typically, the microemulsion method generates particles with a better size distribution for smaller nanoparticles (< ~70 nm) than the Stöber method. The Stöber method is typically used for the generation of bigger nanoparticles (> ~70 nm).

3.2. Synthesis of Silica Nanoparticles

A set of silica nanoparticles was first synthesized by the microemulsion method. In a typical experiment, a nonionic surfactant, Igepal CO-520 (0.44 g) was dissolved in cyclohexane (9 mL) by sonication and vortex. Then, ammonium hydroxide (28% in water, 85 μL) and TEOS (60 μL) were consecutively added to the solution with vigorous stirring. The nanoparticle size was controlled by simply changing the reaction time. The reaction was stopped at 11 hrs, 16 hrs, and 61 hrs for particles with diameters of 21.4 ± 1.6 nm, 30.1 ± 2.7 nm, and 33.1 ± 1.5 nm, respectively. After the reaction, the particles were precipitated by methanol (45 mL), and the precipitates were collected by centrifugation (9000 rpm, 30 min) and redispersed in 10 mL ethanol. The purification procedure was repeated one more time, and the purified particles were dispersed in 10 mL water.

3.3. Shape Evolution of Silica Nanoparticles

The synthesized silica nanoparticles were characterized by transmission electron

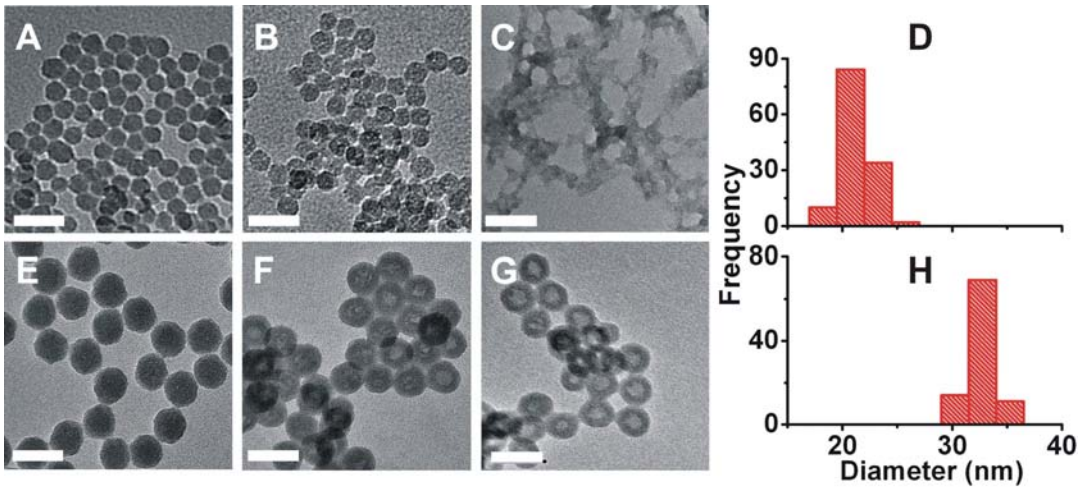

Figure 10. Shape change of silica nanoparticles of two different sizes (A-D: 21.4 ± 1.6 nm, E-H: 33.1 ± 1.5 nm) shown by TEM images after (A, E) 0 day, (B, F) 15 days, and (C, G) 30 days. Scale bar: 50 nm. The diameters of the two different sized particles were determined to be (D) 21.4 ± 1.6 nm and (H) 33.1 ± 1.5 nm particles, respectively. The particles were synthesized by the microemulsion method.

microscopy (TEM) over time to examine the structural integrity and stability of the particles (Figure 10). Interestingly, these small silica particles showed progressive shape changes that were dependent on the particle size. The smallest particles, possessing diameters of 21.4 ± 1.6 nm, initially developed small pores inside the particles, and they were eventually clumped together into featureless aggregates (Figure 10A-10D). No spherical particles of this size were found in the sample after 30 days, indicating that most nanoparticles were either aggregated or dissolved. This transformation is likely due to the high surface energy of the small particles. As shown in Figure 10E-10H, bigger nanoparticles maintain the discrete nature of spherical particles. At the same time, these particles exhibit an interesting shape change from solid spheres into hollow structures. Figure 10E-10G presents the shape evolution of 33.1 ± 1.5 nm particles. Initially, multiple small pores are first developed inside the nanoparticles (Figure 10F), which eventually merge into a void to form hollow nanoparticles (Figure 10G). This behavior was consistently observed with particles possessing similar diameters, as shown with 30.1 ± 2.7 nm (Figure 11) and 43.3 ± 2.2 nm particles (Figure 12).

At a glance, this result is quite surprising considering the chemical stability of silica towards most reactive chemicals. However, it is well-known that OH^- and F^- ions can dissolve silica by coordinating to Si atoms and weakening Si-O bonds.[4] The small amount of ammonium hydroxides remaining in the nanoparticle solution can thus act as

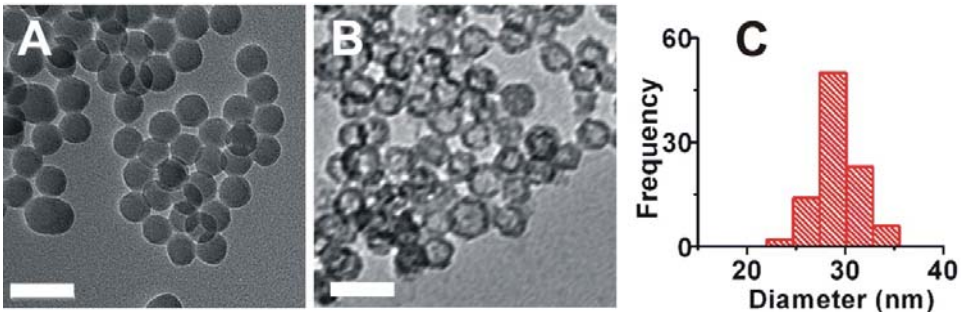

Figure 11. TEM images of silica nanoparticles synthesized by the microemulsion method (A) right after the synthesis and (B) after 30 days (Scale bar: 50nm). (C) The diameter of the particles was determined to be 30.1 ± 2.7 nm.

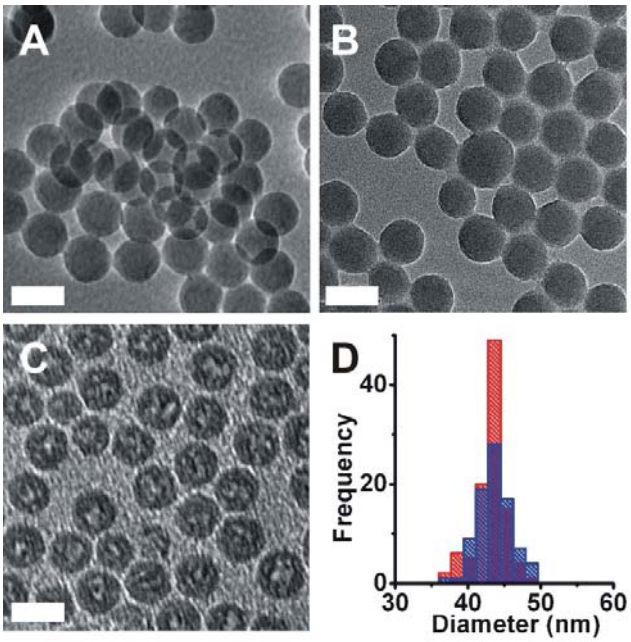

Figure 12. The effect of pH on the shape change of silica nanoparticles monitored by taking TEM images (A) right after the synthesis, (B) after 30 day incubation in an acidic solution (pH 4.0), and (C) after 30 day incubation in a basic solution (pH 10.0). Scale bar: 50nm. (D) Size histograms of the particles shown in (A) (red) and (C) (blue).

an etchant for silica nanoparticles, causing the structural change. To test the hypothesis, we examined the effect of pH on the shape change of silica particles with the diameter of 43.3 ± 2.2 nm. Portions of freshly synthesized silica nanoparticles were kept in dilute acetic acid solution (0.04 M, pH 4.0) and ammonium hydroxide solution (0.04 M, pH 10.0), respectively. The particles were then imaged by TEM with the time interval of 15 days (Figure 12). As shown in Figure 12B, silica particles remain intact in acidic solution even after two months. On the other hand, particles kept in ammonium hydroxide solution started developing pores within 15 days (Figure 12C). The reaction scheme for the dissolution of silica network in basic solution is shown in Scheme 3, where OH^- ions catalyze the hydrolysis of Si-O bonds and solubilize Si-O polymeric networks into monomeric silicic acid, $Si(OH)_4$.[4,14] The pH of the solution of purified nanoparticles that were presented in Figure 10 was 7.5, indicating that this slight basic condition is sufficient to cause the drastic change in the shape of small silica nanoparticles.

Although this observation confirms that the time-dependent shape evolution is caused by the base-catalyzed etching of silica, it does not explain the formation of hollow structure. It is indeed quite intriguing that the etching takes place predominantly in the core part of the particles rather than at the exterior. Based on the local reactant accessibility, particle size should become smaller as the etching reaction proceeds. In addition, once small pores start developing in the core, the concentration of etching

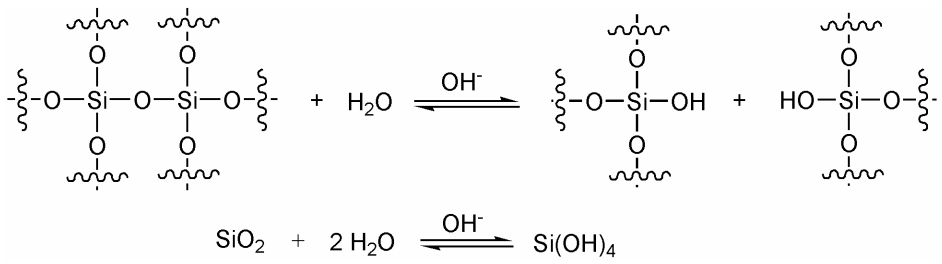

Scheme 3. Dissolution of silica networks by hydroxide ions.

products (silicic acid) should increase in the core of the nanoparticles, which should also slow down the etching reaction in that region. Figure 12D presents the size histograms of the nanoparticles right after the synthesis (red) and after 30 day incubation in a basic solution (pH 10, blue). The diameters of the fresh and aged particles were determined to be 43.3 ± 2.2 nm and 43.9 ± 2.4 nm, respectively, confirming that the overall size of nanoparticles remains similar after the etching reaction.

One possible explanation for this phenomenon is the soft templating effect by the surfactants (Igepal CO-520) used in the synthesis. In this hypothesis, surfactants added to stabilize water-in-oil emulsion might be localized in the core part of the silica nanoparticles. As silica is dissolved away in a slightly basic solution, surfactant molecules escape the particles, leaving a hole inside. To test the hypothesis, we synthesized silica particles by the Stöber method, which does not require surfactants. In a typical experiment, TEOS (750 μL) was injected to ethanol (25 mL) containing ammonium hydroxide (28 %, 1.5 mL) while stirring. The reaction was continued for 24 hrs, and the synthesized silica nanoparticles were collected by centrifugation (9000 rpm, 30 min). The precipitates were subsequently washed with ethanol (40 mL) once and stored in water (5 mL). The particle diameter was determined to be 48.7 ± 4.4 nm by TEM.

Interestingly, the particles prepared by the Stöber method also showed the similar structural change as the ones prepared by the microemulsion method. From the images

presented in Figure 13, it is apparent that small pores are initially developed inside the particles (Figure 13B), and those pores are eventually merged into a big void in the core, generating hollow nanoparticles (Figure 13C). This result clearly indicates that surfactants do not play a role in the shape change, and the hollow structure formation is not the result of soft-templating.

Based on these observations, we hypothesize that the hollow nanoparticles are formed by two steps, the nucleation and growth of pores, in a way similar to the nanoparticle growth process described in Figure 14. In typical nanoparticle syntheses, the nucleation step generates small seed particles, and the seeds grow into bigger particles in the expense of smaller particles with higher surface energy.[15,16] Similarly, in the hollow particle formation described here, small pores are initially formed inside the particles (Figure 14II). Then, the high surface energy of the small pores causes them to collapse into bigger voids to reduce the surface energy (Figure 14III). The bigger voids eventually merge and form hollow nanoparticles (Figure 14IV). The TEM images corresponding to each step of the process are presented in Figure 14A-F. These two step processes were observed with silica particles synthesized by both the Stöber and microemulsion methods (see Figure 10F,G for the microemulsion method and Figure 13B,C for the Stöber method). A series of Si-O bond breaking and making processes by the hydroxide ions[4] might assist the pore rearrangement. Upon the coordination of OH^- ions to the Si atoms, Si-O bonds with high bond strain might break to remove the strain in

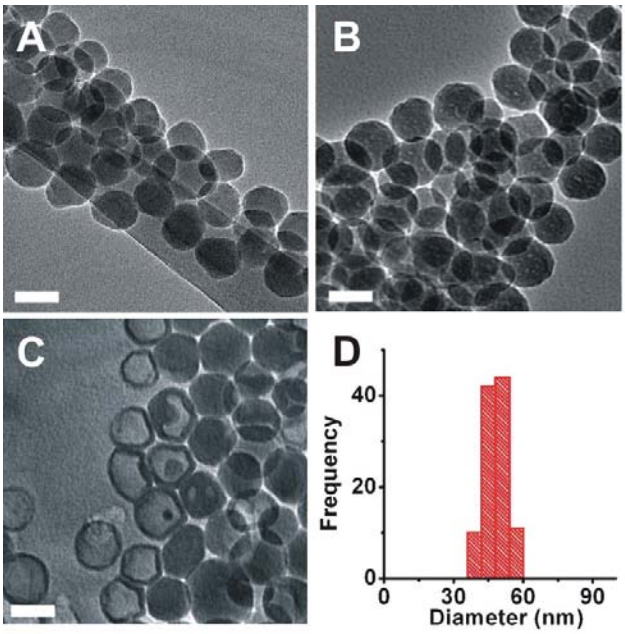

Figure 13. Shape evolution of silica nanoparticles synthesized by the Stöber method. The shape change was followed by taking TEM images after (A) 0 day, (B) 15 days, and (C) 30 days. Scale bar: 50 nm. (D) The diameter of silica nanoparticles was determined to be 48.7 ± 4.4 nm.

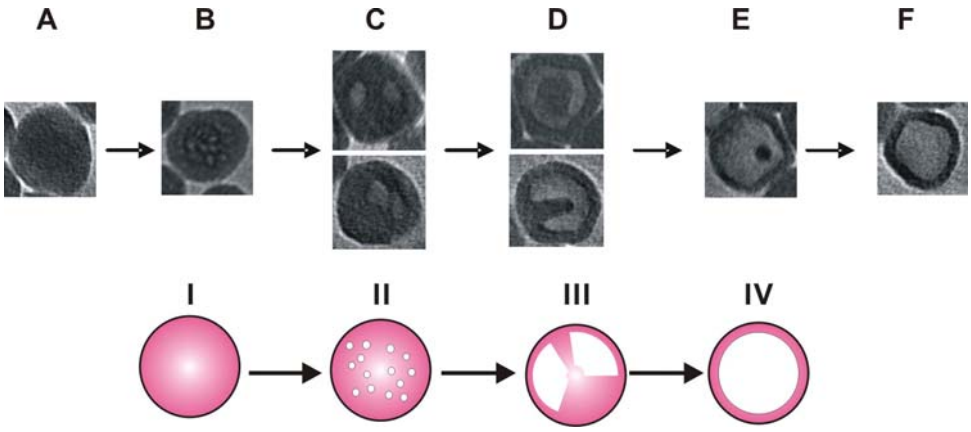

Figure 14. Proposed mechanism for the development of hollow silica nanoparticles.

the Si-O network around small pores, assisting the shape change. In some cases, small silica fragments are observed inside the hollow structure (Figure 14D,E), which are eventually dissolved away to form hollow nanoparticles.

The surface energy and Ostwald ripening have been suggested to play a role during some stages in the formation of hollow structures of crystalline particles for other materials.[10,11] It is worth comparing the mechanism described here with those suggested to explain the formation of other hollow nanostructures, although the reactions involved in the hollow structure formation are different. Alivisatos and coworkers synthesized well-defined hollow nanoparticles of metal chalcogenides based on the Kirkendall effect by reacting crystalline metal nanoparticles with oxygen, sulfur, or selenium.[11] In this work, hollow nanoparticles were developed due to the different diffusion rates between two components. For the system described herein, diffusion should be less important because silica nanoparticles are porous and small molecules can relatively easily diffuse in and out of the particles. If the diffusion rate of reactants and products is an important factor, the etching reaction should be faster at the exterior of the particles, because the reactant (*i.e.*, water and hydroxide ion) concentration should be higher in the solution phase and the product (*i.e.*, silicic acid) concentration should be higher inside the particles, which should lead to reduced particle size rather than hollow nanoparticles. This study demonstrates that the impact of chemical reactions of crystalline and porous nanoparticles can be quite different, which can lead to drastically different shape changes

of nanoparticles. Indeed, the etching of crystalline particles should produce smaller nanoparticles not hollow structures as it has been observed with CdSe quantum dots.[17] In case of porous nanoparticles, the etching reaction can occur throughout the nanoparticles, generating small seed pores inside the particles, as reactants can relatively easily diffuse into the particles. Although it is not visible in TEM images, small pits might be formed on the surface of nanoparticles as well by the etching reaction. However, the surface energy of the pits on the nanoparticle surface should be lower than that of small pores inside the nanoparticles, which would result in a faster etching reaction in the core. It is also possible that the seed pores are preferentially formed inside the silica particles due to the density variation in different regions of silica particles. Nonetheless, it is the porous nature of the particles that allow for the formation of seed pores in the core, which eventually feed into the hollow space in the core region of the particles. This study clearly demonstrates that in porous materials the shape change is dominated by the surface energy.

This behavior is unique to nanoparticles, and the shape change is highly size-dependent. Nanoparticles in the size range of 30-50 nm are shown to be transformed into well-defined hollow structures. Larger silica particles with the diameter of 123.1 nm $\pm$ 9.4 nm were also prepared by the Stöber method. The synthetic conditions were similar to those used to make 48.7 nm particles shown in Figure 13 except that the reaction time was longer (30 hrs). Those larger particles also developed small internal pores (Figure

15). However, hollow structures were not formed even after 2 months. As shown in Figure 10A-10C, smaller particles with diameters of 21 nm tend to aggregate with each other.

3.4. Conclusion

This study is important for the following reasons. First, the mechanism described herein provides an easy and efficient way to prepare hollow nanostructures of porous materials. Indeed, while synthetic methods for making nanoparticles with various shapes and sizes have been greatly advanced for the past decade, it is still challenging to generate hollow structures without the use of templates. The ability to control the porosity and local environment of silica nanoparticles is undoubtedly important in many applications including catalysts and drug delivery. Second, this study reinforces the importance of studying materials properties at different size ranges. In the current study, we show that the trivial reactivity of silica in dilute basic solution can lead to a drastic morphology change of silica nanoparticles. Silica particles have been widely used in a variety of applications including biological imaging, and it is important to assess their structural integrity and chemical stability for these applications. This study also points out that better surface passivation methods should be implemented for applications of small silica particles (< 50 nm) where the stability of silica particles is critical. Finally, the mechanism of hollow structure formation described here should be applicable to other technologically important materials such as TiO_2 and SnO_2.

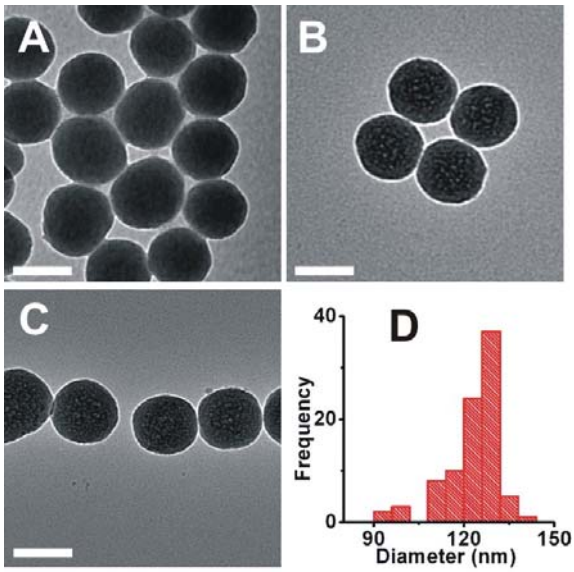

Figure 15. TEM images of silica nanoparticles synthesized by the Stöber method (A) right after the synthesis, (B) after 15 days, and (C) after 30 days. (Scale bar: 100 nm). (D) The diameter of the particles was determined to be 123.1 ± 9.4 nm.

3.5. Reference

(1) Thomas, J. M.; Johnson, B. F. G.; Raja, R.; Sankar, G.; Midgley, P. A. *Acc. Chem. Res.* **2003,** 36, 20.

(2) Kim, J.; Lee, J. E.; Lee, J.; Yu, J. H.; Kim, B. C.; An, K.; Hwang, Y.; Shin, C.-H.; Park, J.-G.; Kim, J.; Hyeon, T. *J. Am. Chem. Soc.* **2006,** 128, 688.

(3) Ow, H.; Larson, D. R.; Srivastava, M.; Baird, B. A.; Webb, W. W.; Wiesner, U. *Nano Lett.* **2005,** 5, 113.

(4) Iler, R. K., *The chemistry of silica: solubility. polymerization, colloid, and surface properties, and biochemistry*. John Wiley & Sons: New York, 1979.

(5) Sayari, A.; Hamoudi, S. *Chem. Mater.* **2001,** 13, 3151.

(6) Scott, B. J.; Wirnsberger, G.; Stucky, G. D. *Chem. Mater.* **2001,** 13, 3140.

(7) Caruso, F.; Caruso, R. A.; Mohwald, H. *Science* **1998,** 282, 1111.

(8) Darbandi, M.; Thomann, R.; Nann, T. *Chem. Mater.* **2007,** 19, 1700.

(9) Obare, S. O.; Jana, N. R.; Murphy, C. J. *Nano Lett.* **2001,** 1, 601.

(10) Xiong, Y.; Wiley, B.; Chen, J.; Li, Z.-Y.; Yin, Y.; Xia, Y. *Angew. Chem. Int. Ed.* **2005,** 44, 7913.

(11) Yin, Y.; Rioux, R. M.; Erdonmez, C. K.; Hughes, S.; Somorjai, G. A.; Alivisatos, A. P. *Science* **2004,** 304, 711.

(12) Stöber, W.; Fink, A.; Bohn, E. *J. Colloid Interface Sci.* **1968,** 26, 62.

(13) Osseoasare, K.; Arriagada, F. J. *Colloids Surf.* **1990,** 50, 321.

(14) Greenberg, S. A. *J. Phys. Chem.* **1957,** 61, 960.

(15) Murray, C. B.; Kagan, C. R.; Bawendi, M. G. *Annu. Rev. Mater. Sci.* **2000,** 30, 545.

(16) Yin, Y.; Alivisatos, A. P. *Nature* **2005,** 437, 664.

(17) Yu, W. W.; Qu, L. H.; Guo, W. Z.; Peng, X. G. *Chem. Mater.* **2003,** 15, 2854.

Part III

Synthesis and Assembly of Block Copolymers Containing Electronically Active Blocks

4.1. Introduction

Conjugated polymers have emerged as an important class of materials that can replace inorganic semiconductors for a range of applications including solar cells and light emitting diodes owing to their excellent optoelectronic properties and processibility.[1-3] In contrast to their inorganic counterparts, conjugated polymers exhibit complicated optical and transport properties that are highly dependent on their nanometer scale morphology and impurities.[4] While these phenomena open critical problems for device fabrication, they offer a unique opportunity for creating new tunable and responsive materials.

Especially the rod-coil block copolymers consisting of rigid conjugated polymers and flexible insulating polymers have been an intense research topic[5] because the mechanical and processing properties of the conjugated polymers should be enhanced to facilitate the fabrication of the device. Also the block copolymers can be easily self-assembled into various structures from lamellae to sphere to cylinder to vesicle. It gives us more chances to produce the novel optical and electrical nano-devices, impossible or

difficult from the existing methods. The optical and electrical properties of the conjugated polymers strongly depend on their morphologies and as one example the well-interconnected nanofibriles of polythiophene show high electrical performance[6]. Therefore it is very important to elucidate the correlation between their optoelectrical properties and the self-assembled structures.

However, the study of self-assembly of rod-coil block copolymers is intrinsically more difficult than that of well-studied coil-coil block copolymers. The polymers have the strong π-π interaction between the rod blocks and induce the anisotropic ordering. Then it is important to develop methodologies to easily probe the structure and the corresponding properties. Of them the optical properties including absorption, emission, and life time measurements are the powerful tools to study the energy profile of conjugated block copolymers.[7] The different block copolymer morphologies induce the different conformations and energy states of the conjugated backbone and are reflected by different optical properties. The shifting of absorption and emission is mostly caused by aggregation types and conjugation lengths. Of them the latter can produce huge shifting of the optical properties due to disruption of planarity by rotational defect or distortion of conjugated backbone. Therefore, it is a crucial issue to find a proper material to show the distinct optical properties corresponding to the morphologies.

Among the conjugated polymers, polythiophenes and their derivatives including poly(3-alkylthiophene) are one class of the most studied and important materials for both

academies and industries and then various synthetic approaches have been developed to facilitate the synthesis and functionalization.[8] In the terms of optical properties the emission wavelength of polythiophene can cover whole visible range from blue to red and the block copolymers consisting of polythiophene could be a proper material in order to study the correlation between the structures and their optical properties.

Herein, I describe the synthesis of a novel amphiphilic block copolymer composed of a widely used conjugated polymer, poly(3-octylthiophene) and a hydrophilic polymer, poly(ethylene oxide) (POT-*b*-PEO) in order to manipulate the morphology and properties of polythiophene in a highly controllable manner. In this approach, the molecular packing and nanoscale morphology of polythiophene are controlled by utilizing the nature of block-copolymers to self-assemble into a variety of well-defined nanostructures. Importantly, the supramolecular assemblies of POT-*b*-PEO exhibit highly tunable photoluminescent (PL) colors spanning from blue to red depending on their self-assembly structure. Various rod-coil block-copolymers containing π-conjugated oligomers and polymers have been previously synthesized.[9-16] However, most previously reported amphiphilic molecules including block-copolymers of oligothiophenes and polyethylene oxides show spectral red shifts associated with polymer aggregation, which are usually accompanied by significant PL intensity drops.[17] This work is the first to exhibit the wide range of photoluminescence colors obtained through the self-assembly of conjugated block-copolymers.

In addition, this study was extended to present the detailed study of the optical properties dependent on solvent media, block lengths of PEO segments, and interaction of PEO with metal cations. This study demonstrates the importance of the structure-dependent optical properties of conjugated polymers and further suggests an efficient way to tune the optical properties of materials by self-assembly strategy of block copolymers.

4.1.1. Synthesis and Self-Assembly of Polythiophenes

Polythiophenes are one of the most studied and important classes of conjugated polymers. Various synthetic methods, easy functionalization, and unique electronic properties that can be widely tuned result in a tremendous interest on this class of polymers for optoelectronic applications. Especially, the emissive colors in polythiophenes can be easily tuned by suppressing the aggregation effect in the solid state and changing the effective conjugation length in the solution state.[8]

Polymerization of thiophenes can be carried out in various synthetic methods including electropolymerization,[18] metal-catalyzed coupling reactions,[19] and chemical oxidative polymerization.[20] Meanwhile, the solubility of unsubstituted polythiophenes is very poor and once the polymer is prepared it is difficult to further process it as a material for electronic application. The solubility can be greatly enhanced by introduction of side chains and the most widely studied side chains are *n*-alkyl substituents. The metal-

catalyzed coupling reaction of thiophenes has been applied in synthesis of a wide range of poly(3-alkylthiophene)s due to the very high yield, easy introduction of the *n*-alkyl substituents, and facile control of regioregularity of the side groups.

The McCollough method[21] was the first synthesis of regioregular poly(3-alkylthiophenes)s and later was modified as the Grignard metathesis (GRIM) method.[22] One strong advantage of this method is that the use of both cryogenic temperatures and highly reactive metals is unnecessary and then it offers fast and easy preparation of regioregular poly(3-alkylthiophenes)s. This reaction is based on regiospecific metallation of 2,5-dibrom-3-alkylthiophene with Grignard reagent. The Grignard derivatives are polymerized with catalyst of Ni(dppp)Cl_2 using Kumada cross-coupling method. Other methods for preparing regioregular poly(3-alkylthiophenes)s include Rieke method[23] to use highly reactive Rieke zinc that reacts with 2,5-dibrom-3-alkylthiophene instead of Grignard reagents and Stille[24] and Suzuki[25] palladium-catalyzed cross-coupling reactions.

The discovery of the synthesis of regioregular poly(3-alkylthiophenes)s has brought about the development of a wide variety of new functional polythiophenes. Also the electrical properties of regioregular poly(3-alkylthiophenes)s has been dramatically enhanced due to planarization of the backbone and solid-state self-assembly to form well-defined, organized three-dimensional polycrystalline structures.[26] These structures provide efficient interchain and intrachain charge carrier pathways, leading to high conductivity. Therefore, polymer structures are crucial for the determining the

optoelectrical properties of conjugated polymers. It is important that design, synthesis, and assembly be taken into account in the optimization of organic optoelectronic devices.

4.1.2. Synthesis and Self-Assembly of Conjugated Block Copolymers

The self-assembly of block copolymers into a nanostructure with novel morphology and property has attracted extensive interest as a new approach for advanced applications in materials science, chemical synthesis, and nanofabrication.[9,27] The assembly characteristics of coil-coil block copolymers depend on the morphological transformation, which is determined by the relative block length, block polarity, volume fraction, chain flexibility, temperature, polymer concentration, mixed solvent composition, and so on. Recently, rod-coil block copolymers have received a great deal of attention since they offer an attractive strategy for the organization of rod-like polymers such as conducting polymers with rigid π-conjugated backbones. In particular, block copolymers containing conducting polymer segments, polyfluorene,[28,29] poly(phenylene vinylene),[30,31] and polythiophene,[14,16] have been reported in the literature.

Aggregation and microphase separation of rod-coil block copolymers have yielded a number of nanoscale morphologies, such as lamellar, spherical, cylindrical, vesicular, and microporous structures.[5] The π-π interaction between the conjugated rods provides additional control factor and functionality, which differs distinctly from those of conventional coil-coil block copolymers. Furthermore, the self-assembled morphology of

conjugated rod-coil block copolymers may lead to additional electronic processes such as excition confinement and interfacial effects. Also, the combination of a stimuli-responsive coil segment with the tunable photophysical properties of the conjugated rod could produce novel multifunctional sensory materials.

For some examples, Yu and co-workers have prepared a series of rod-coil block copolymers based on oligo(phenylene vinylene) (OPV) and poly(ethylene glycol) (PEG).[30] These polymers organized into cylindrical micelles in solution and in cast films on a nanometer scale, which have a cylindrical OPV core surrounded by a PEG corona. McCullough and co-workers described the synthesis and nanowire morphologies of conjugated block copolymers consisting of poly(3-alkylthiophene) and poly(styrene) or poly(acrylate).[14] Su and co-workers synthesized poly(3-hexylthiophene) (P3HT)-*block*-poly(2-vinyl pyridine) (P2VP) copolymers and showed that the block copolymers microphase separate and self-assemble into nanostructures of sphere, cylinder, lamellae, and nanofiber structures according to different P2VP volume fractions.[16]

However, all the studies from the previously reported conjugated rod-coil block copolymers have focused on the morphological transformation through control of molecular components and lengths. There are few reports to show the enhancement or modulation of their optical and electrical properties through accurate control of polymer morphology in a predetermined way.

4.2. Experimental Section

Materials: Methanol, hexanes, and chloroform were purchased from Fisher Scientific. All other reagents were purchased from Aldrich. Distilled THF was used for all the synthesis to ensure anhydrous reaction conditions. Ethylene oxide was dried by passage through NaOH packed column followed by distillation over CaH_2. All other reagents were used without further purification.

Instrumentation: ^1H NMR spectra were obtained using Bruker 500 MHz spectrometer in $CDCl_3$ solvent. Chemical shifts were reported in ppm relative to the solvent residual proton ($\delta = 7.24$). GPC measurements were carried out at 40^oC on a Shimadzu LC-10AT liquid chromatography system equipped with two series of Resipore 300X7.5MM columns (Varian Inc.) and SPD-10AVvp absorbance UV/Vis detector. THF was used as the eluent at a flow rate of 1.0 mL/min. Calibration was based on poly(styrene) standards (Polymer Laboratories). MALDI-TOF MS (Voyager) was used to measure molecular weights in positive mode. The matrix used was 2, 2': 5, 2''-terthiophene (Aldrich). Fluorescence emission measurements were recorded with a Fluorolog®-3 spectrofluorometer (HORIBA Jobin Yvon, Inc.) utilizing an R928 PMT detector. For all the spectra measurements, POT-*b*-PEO in solution was assumed to have the same extinction coefficient as POT ($\varepsilon = 7.4 \times 10^3$ $cm^{-1}M^{-1}$)[32] and the extinctions were converted into the molar concentrations of the polymers. The emission spectra were integrated and the calculated values were used for the comparison of the emission

intensities. Fluorescence lifetime measurements were performed using a time-correlated single-photon counting (TCSPC) technique. The TCSPC system consisted of a pulsed picosecond diode laser (Picoquant GmbH) generating 20 MHz output pulses at 405 nm, a subtractive double monochromator with a MCP-PMT (Hamamatsu R2809U) detector, and a TCSPC board (Becker & Hickl, SPC-730). The instrument response of the system was ~80 ps (FWHM). Decay curves were collected at 560 nm emission wavelength and were analyzed using FluoFit software (Picoquant GmbH) via an iterative reconvolution method. Transmission electron microscopy (TEM) was performed on a JEOL TEM-2010F operating at 200 kV accelerating voltage.

Synthesis of Hydroxyl-Terminated POT: The hydroxyl-terminated POT was synthesized following a previously reported method (Scheme 4).[33,34] First, vinyl-terminated POT was synthesized by Grignard metathesis (GRIM) method developed by McCullough and coworkers and it was subsequently converted into hydroxyl-terminated POT by hydroboration and oxidation reactions.[34] Synthesized polymers were purified by a series of Soxhlet extraction using hexanes, methanol, and chloroform, and then characterized by NMR and MALDI. The molecular weight (M_n) and the degree of polymerization (DP) of synthesized POT were determined to be 3000 g/mol and 15 by MALDI spectroscopy.

Synthesis of POT-*b*-PEO Block Copolymers: The POT-*b*-PEO was synthesized by initiating the anionic ring-opening polymerization of ethylene oxide (EO) at the end of

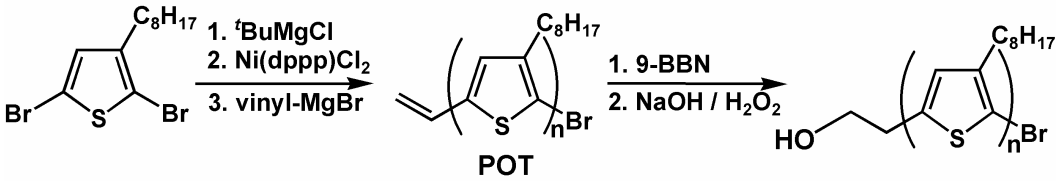

Scheme 4. Synthesis of hydroxyl-terminated POT.

hydroxyl-terminated POT (Scheme 5). It was critical to carry out the reaction in a moisture-free environment. In typical experiments, ethylene oxide was first dried by passing through NaOH-filled column. To further remove the residual amount of water, the dried ethylene oxide was collected into a round bottom flask containing CaH_2 by using acetone-dry ice bath, and distilled into a graduated Schlenk tube. (Figure 16) In a separate round bottom flask, hydroxyl-terminated POT was dissolved in THF (0.5 mg/mL, 20 mL). Potassium naphthalide (0.95 M in THF) was added drop wise to the solution until the solution color remains light green, which is indicative of the presence of potassium naphthalide in slight excess. Finally, measured amounts of ethylene oxide were transferred to the reaction vessel containing hydroxyl-terminated POT through cannula. The amounts of ethylene oxide used for the syntheses were 2.0, 2.2, 3.5, 6.0, and 9.0 mL for POT_{15}-*b*-PEO_{38}, POT_{15}-*b*-PEO_{42}, POT_{15}-*b*-PEO_{55}, POT_{15}-*b*-PEO_{70}, and POT_{15}-*b*-PEO_{150}, respectively. The anionic polymerization of PEO was carried out at room temperature under stirring. The reaction was terminated after 48 h by the addition of HCl (the same volume as used potassium naphthalide, 1.0 M in diethyl ether). Then, cold diethyl ether (~100 mL) was poured into the solution to precipitate out the reaction product. The precipitates were recovered by filtration or decantation. In some cases, especially block copolymers with low molecular weight, the flask was put on the table and after the precipitate was settled down on the bottom, the supernatant was decanted by pipette. Then cold diethyl ether was added into the precipitate and the supernatant was

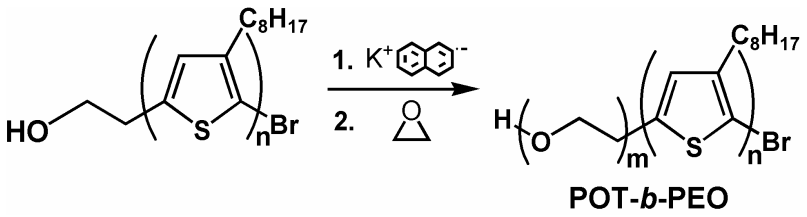

Scheme 5. Synthesis of POT-*b*-PEO block copolymers.

Figure 16. Pictures to show the experimental set-ups to collect ethylene oxide (left) and the cryo-distill the collected ethylene oxide into a graduated Schlenk tube (right).

decanted. This process was repeated several times. The collected product by filtration or decantation was redissolved in chloroform. The undissolved solid in chloroform was removed by filtration. Chloroform was subsequently removed via rotary evaporator, and the remaining POT-*b*-PEO product was dried under vacuum overnight. The dried product was then dispersed in methanol (~ 20 mL) to remove residual amount of unreacted POT. Finally, purified POT-b-PEO was dried in vacuum and stored in dark. The molecular weights and PDIs of the synthesized POT-*b*-PEO are shown in Table 1. ^{1}H NMR (500 MHz, $CDCl_3$) of POT_{15}-*b*-PEO_{38} δ: 0.87 (t, 3H, *J* = 6.85 Hz), 1.27 (m, 10H), 1.67 (m, 2H), 2.78 (t, 2H, *J* = 6.75 Hz), 2.98 (t, 2H, *J* = 7. 09 Hz), 3.60 (s, 214H), 4.29 (2H, t, *J* = 4.18 Hz), 6.97 (1H, s).

Quantum Yield Measurements

The quantum yields of POT_{15}-*b*-PEO_{38} in THF, methanol, and water were determined following the typical procedure described in the previous report.[18] Coumarin 102 (ethanol) with QY of 95 %[19] was used as a standard for all three samples. UV/Vis and PL spectra were obtained for a series of dilute samples of POT_{15}-*b*-PEO_{38} in different concentrations. The absorbance was kept lower than 0.055 for all QY measurements to avoid the self-quenching. The methanol samples were excited at 364 nm, and THF and water samples were excited at 400 nm. The entire set of measurements was repeated three or four times for each sample. The quantum yields were determined

Table 1. Synthesized POT-*b*-PEO block copolymers

Block copolymer	M_n (PEO) (g/mol)	DP of PEO	f_{PEO}	PDI[+]
POT_{15}-*b*-PEO_{38}	1670	38	0.36	1.5
POT_{15}-*b*-PEO_{42}	1850	42	0.38	1.5
POT_{15}-*b*-PEO_{55}	2420	55	0.45	1.5
POT_{15}-*b*-PEO_{70}	3080	70	0.51	1.2
POT_{15}-*b*-PEO_{150}	6600	150	0.69	1.2

[+]The PDI was obtained by using GPC data, which provide upper limits of the true PDI for rod-like polymers.[31]

to be 18 ± 1.3, 12 ± 1.3, and 1.6 ± 0.33 % for THF, methanol, and water samples, respectively. The actual QY of the water sample should be somewhat higher than the determined value of 1.6 % because the potential effect of light scattering on the extinction and the PL spectra was ignored in the QY estimation. Scattering was not significant for the methanol sample at low concentrations used for quantum yield measurements as indicated by the low extinction at the long wavelength range (Figure 17). Note that the QY of the assemblies in methanol remains relatively high. In addition, the absorbance measured at the same concentration is higher for the methanol sample than the THF sample (Figure 17). Thus, both the relatively high QY and high absorption contribute to the strong PL intensity of the assemblies in methanol.

4.3. Synthesis of POT-*b*-PEO Block Copolymers

The POT-*b*-PEO block-copolymers were synthesized by initiating the anionic ring-opening polymerization of ethylene oxide (EO) at the end of hydroxyl-terminated poly(3-octylthiophene) (POT) (Scheme 4 and 5). The hydroxyl-terminated POT was synthesized following a literature procedure developed by McCullough and coworkers.[34] The molecular weight (*Mn*) and polydispersity index (PDI) of POT were determined to be 3000 (g/mol) and 1.24 by matrix-assisted laser desorption/ionization (MALDI) spectroscopy. A set of POT-*b*-PEO with different PEO lengths was synthesized using the same batch of POT in order to examine the effect of relative block lengths on the self-

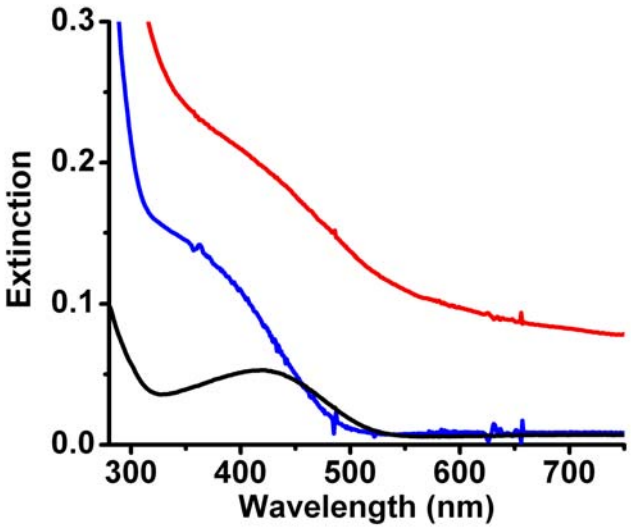

Figure 17. UV/Vis extinction spectra of POT_{15}-*b*-PEO_{38} at a low concentration (0.25 g/L) in THF (black), methanol (blue), and water (red). Extinction coefficients were estimated to be 1300 $M^{-1}cm^{-1}$ at 419 nm and 3100 $M^{-1}cm^{-1}$ at 364 nm for isolated block-copolymers in THF and the assemblies in methanol, respectively.

assembly. The molecular weights and PDIs of the synthesized POT-*b*-PEO are shown in Table 1. Subsequently, the anionic ring opening polymerization of EO was initiated at the hydroxyl end-group of POT by using potassium naphthalide as an initiator to produce POT-*b*-PEO. Because GPC overestimates the molecular weight of rigid conjugated polymers, the number-averaged molecular weights of PEO blocks were determined by NMR end-group analysis using the peak of methylene proton right next to the POT block and the proton peaks of PEO chains as described in Figure 18. Figure 19 presents GPC spectra of the synthesized POT-*b*-PEO polymers. Although GPC data do not provide accurate estimation of molecular weights of conjugated block-copolymers, they still provide means of qualitative comparison and show that the trends observed by NMR and GPC are consistent. The gradual reduction of retention time with increasing lengths of PEO also confirms that POT and PEO blocks are indeed physically connected.

The polythiophene is electron-rich and can be easily oxidized under some conditions. To check if the reaction condition has the highly oxidation potential the unreacted POT molecules after anionic polymerization of PEO block were collected and the emission spectra were measured and compared with pristine POT. (Figure 20) The recorded emission spectra were consistent to that of pristine POT and it excludes the possibility to be oxidized during the synthesis.

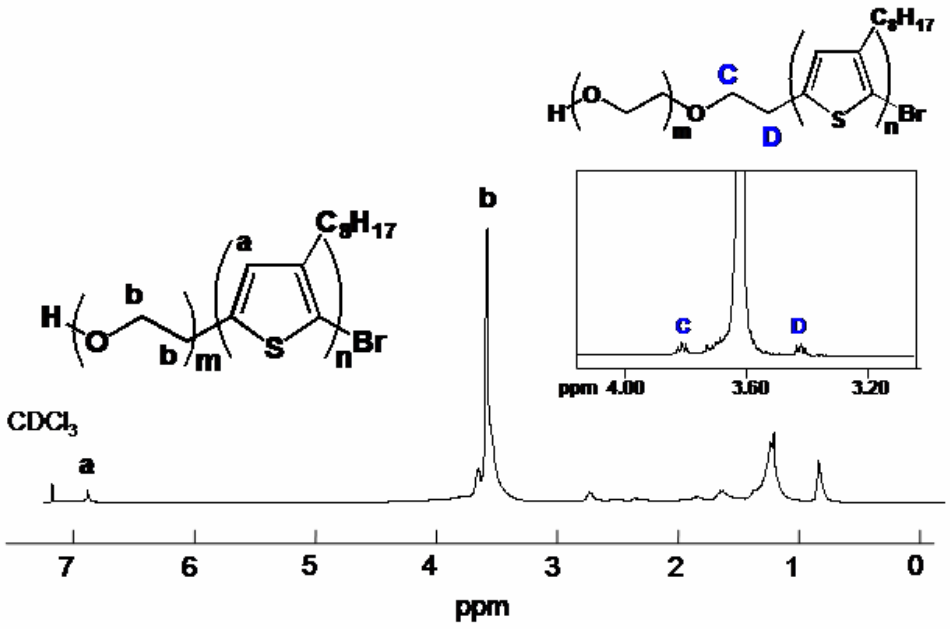

Figure 18. Representative ^{1}H NMR spectrum of POT_{15}-*b*-PEO_{38} in $CDCl_3$.

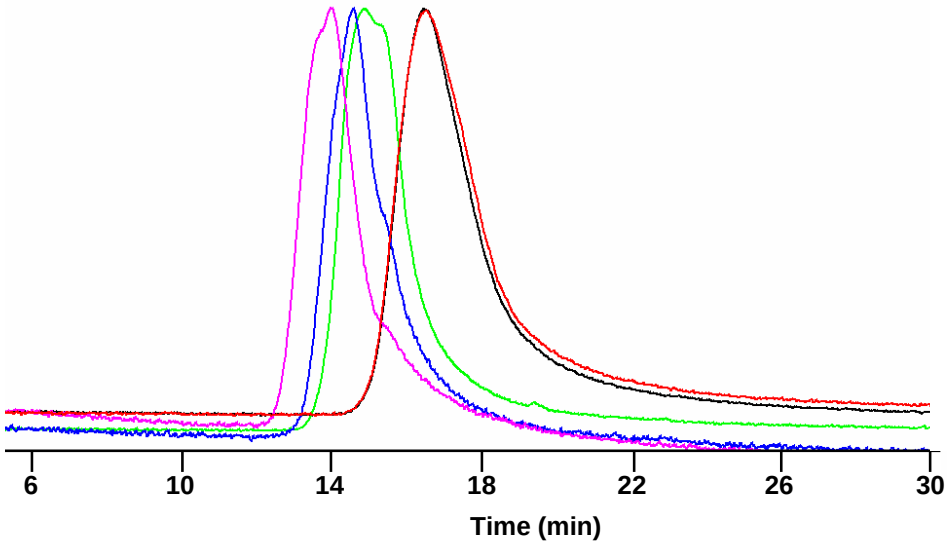

Figure 19. Gel Permission Chromatography (GPC) of POT-*b*-PEO. Black: POT_{15}-*b*-PEO_{38}, Red: POT_{15}-*b*-PEO_{42}, Green: POT_{15}-*b*-PEO_{55}, Blue: POT_{15}-*b*-PEO_{70}, and Cyan: POT_{15}-*b*-PEO_{150}.

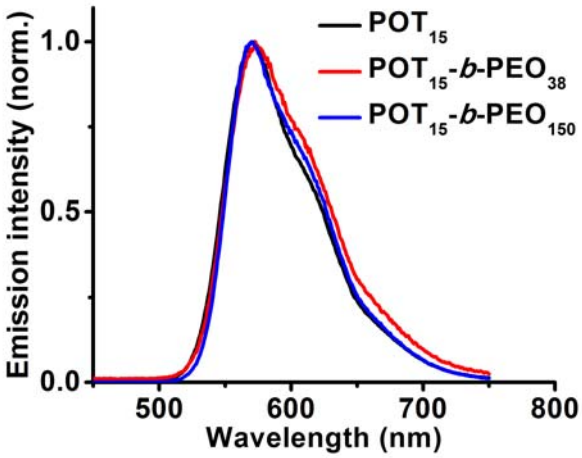

Figure 20. Emission spectra of the unreacted POT during anionic polymerization and removed during purification.

4.4. Self-Assembly and Optical Properties

4.4.1. POT_{15}-*b*-PEO_{38} Copolymers

The as-synthesized POT_{15}-*b*-PEO_{38} block copolymers were dispersible in a wide range of solvents due to the amphiphilic nature of the polymer (Figure 21A). In contrary, the solubility of POT homopolymers in polar solvents such as alochols and water is so poor that the polymer exists as the aggregated soild phase not to produce any significant emission due to the strong interchain energy trasfer. (Figure 21B) The emissive colors and spectral features of POT_{15}-*b*-PEO_{38} are highly dependent on the polarity of solvents. The POT_{15}-*b*-PEO_{38} in THF and chlroform having the similar polarity shows the simiar emission spectra (Figure 22). Also all the alcohols including methanol, ethanol, and propanol exhibit the small shifting of emission spectra and the same emission colors under UV illumination. (Figure 22)

In non-selective good solvents such as THF, POT_{15}-*b*-PEO_{38} exists mostly as isolated molecules and show emission properties similar to that of homopolymers of POT, emitting orange colored light under the UV illumination (Figure 23A). In selective polar solvents such as water and methanol, POT_{15}-*b*-PEO_{38} self-assembled into core/shell type nanostructures with POT in the core and PEO in the shell, exposing hydrophilic PEO at the exterior. As presented in Figure 23C, spherical assemblies were formed in water along with ordered superstructures of the spherical assemblies. In methanol, POT_{15}-*b*-PEO_{38} self-assembled into fiber-like structure (Figure 23B). Both

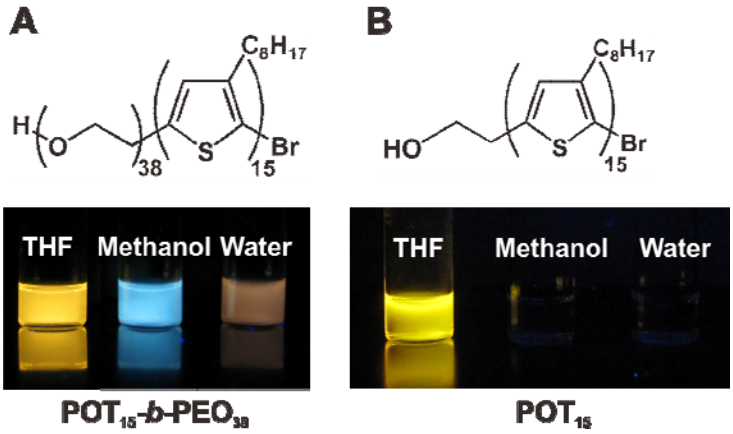

Figure 21. Emission colors of (A) POT_{15}-*b*-PEO_{38} and (B) POT_{15} in THF, methanol, and water under UV light.

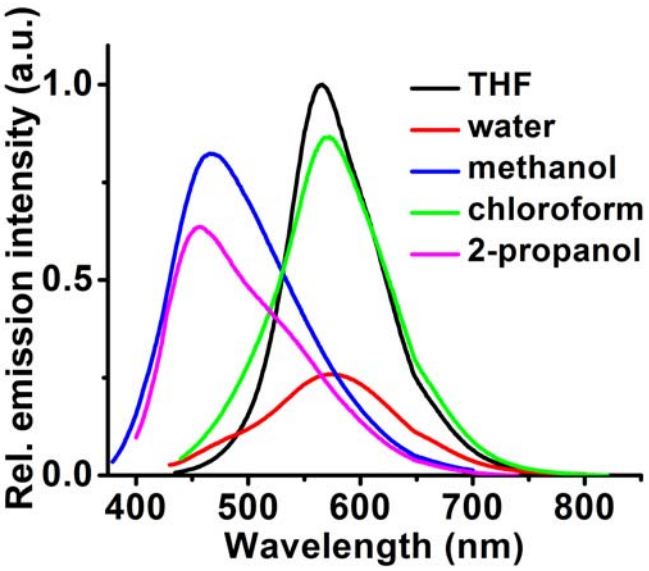

Figure 22. Emission spectra of POT_{15}-*b*-PEO_{38} (2.7×10^{-5} M) in THF (black, λ_{ex} = 420 nm), water (red, λ_{ex} = 400 nm), methanol (blue, λ_{ex} = 360 nm), chloroform (green, λ_{ex} = 420 nm), and 2-propanol (cyan, λ_{ex} = 380 nm).Each sample was excited at its corresponding excitation maximum.

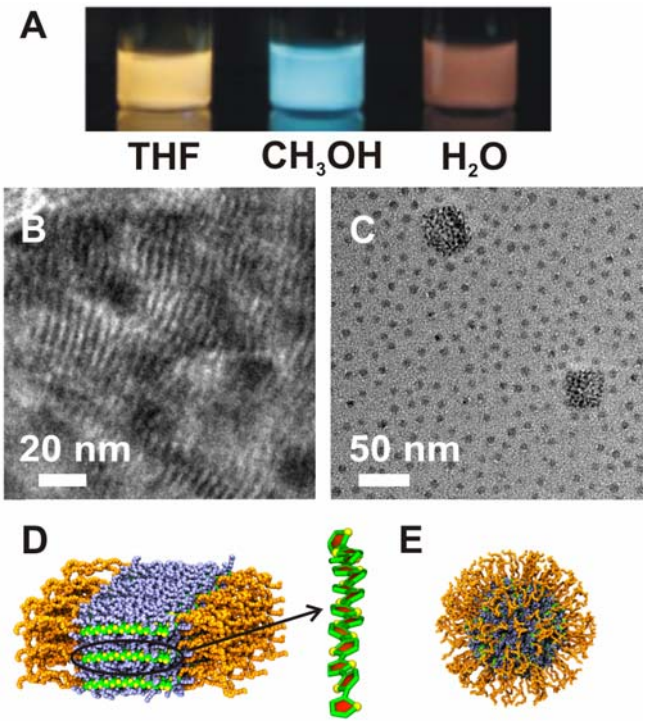

Figure 23. (A) Distinct emission colors of POT_{15}-*b*-PEO_{38} in three different solvents under UV-illumination. (B-C) TEM images of POT_{15}-*b*-PEO_{38} assemblies in methanol (B) and in water (C). (D-E) Structural models showing PEO (orange), octyl side chain (ice blue), and polythiophene backbone (carbon: green, sulfur: yellow) for methanol (D) and water (E) samples.

isolated and bundled fibers were observed. The distinct morphologies observed in water and methanol can be explained by the relative volume change in different solvents; as the relative volume of PEO becomes smaller in methanol,[35] POT_{15}-*b*-PEO_{38} forms fiber-like assemblies with less interfacial area.[5]

Remarkably, the light emitting properties of POT_{15}-*b*-PEO_{38} were highly dependent on the self-assembly structure (Figure 24). Aqueous suspension of POT_{15}-*b*-PEO_{38} assemblies showed a red-colored emission under UV illumination (Figure 23A) with a slightly red-shifted spectrum due to the energy transfer to low energy sites[36] in the packed POT strands (Figure 24A). The red-shift was accompanied by reduced PL intensity. The spectral red shift and the decrease in quantum yields are well-documented phenomena of conjugated polymer aggregates and thin films.[8,17] Interestingly, POT_{15}-*b*-PEO_{38} showed a drastic color change in methanol and exhibited a strong blue emission (Figure 23A and Figure 24A).

The PL quantum yields (QY) of the assemblies in methanol and isolated molecules in THF were determined to be 12 % and 18 %, respectively, showing that the QY remains relatively high in the self-assembled structure in methanol. This behavior is distinct from the significantly reduced QYs shown for aggregates of other conjugated amphiphiles.[10,37] In addition, the assemblies in methanol absorb light more strongly than isolated molecules in THF (Figure 17). Both the relatively high QY and the high absorption coefficient contribute to the strong PL intensity of the assemblies in methanol.

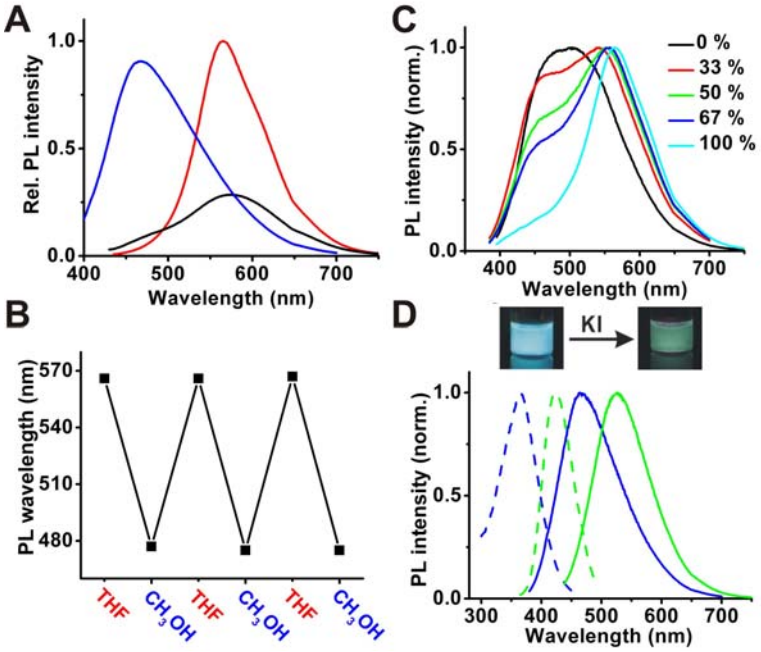

Figure 24. (A) PL spectra of POT_{15}-*b*-PEO_{38} (2.7×10^{-5} M) in THF (red, λ_{exc}= 419 nm), methanol (blue, λ_{exc}= 364 nm), and water (black, λ_{exc}= 396 nm). Each sample was excited at their respective excitation maxima. (B) Reversible PL wavelength changes in THF and methanol (λ_{exc}= 380 nm). (C) PL spectra of POT_{15}-*b*-PEO_{38} in THF/methanol solvent mixtures at a series of different THF volume percent (λ_{exc}= 380 nm). (D) Excitation (dashed) and emission (solid) spectra of POT_{15}-*b*-PEO_{38} in methanol without (blue) and with (green) KI (0.07 M).

The spectral blue-shift in the assembly structure is attributed to the reduced conjugation length caused by the rotational defects (*i.e.*, disruption of planarity by twists) in the assembly structure. Consistent with the hypothesis, there is no well-defined vibronic structure at the absorption edge which typically appears in well-packed polythiophene aggregates (Figure 25).[38] The absorption peak position is blue-shifted for the methanol sample due to the reduction of the conjugation length. The tails in the long wavelength range of the methanol and the water samples indicate the formation of large assemblies of conjugated block copolymers and are consistent with TEM (Figure 23) and DLS (Figure 26) results. The simple solvochromic effect cannot account for the observed spectral shift; poly(3-octylthiophene) homopolymers exhibit red-shifted spectrum in methanol/THF mixtures because the polymer adopts more planar conformation in poor solvents (Figure 27 and 28).

The study was further extended into the measurement of emission spectra according to a series of excitation energy. The POT_{15}-*b*-PEO_{38} in THF and water shows the same emission spectra irrespective of excitation wavelengths (energies) and indicates that the polymers exist as a single emitter in those solutions. (Figure 29A and 29C) In contrary, the emission wavelength of the methanol sample shows the continuous shifting of emission peak positions with shifting of the excitation wavelengths (Figure 29B), indicating that the polymers act as multiple emitters and have a distribution in conjugation lengths. This observation also supports our structural model that the POT

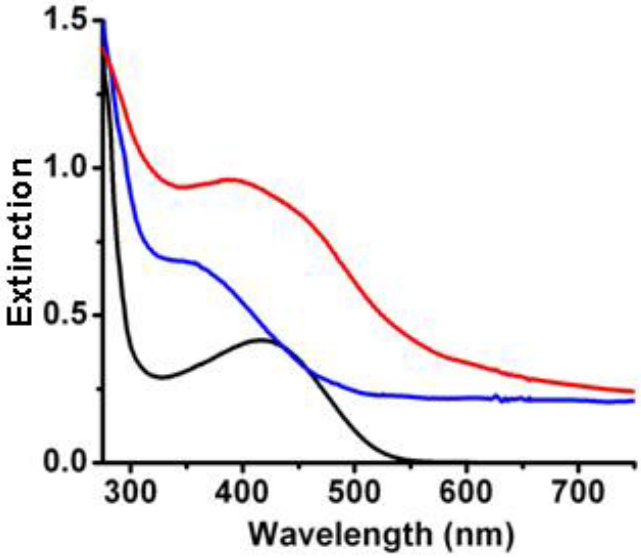

Figure 25. UV/Vis extinction spectra of POT_{15}-*b*-PEO_{38} (2.5×10^{-4} M) in THF (black), methanol (blue), and water (red).

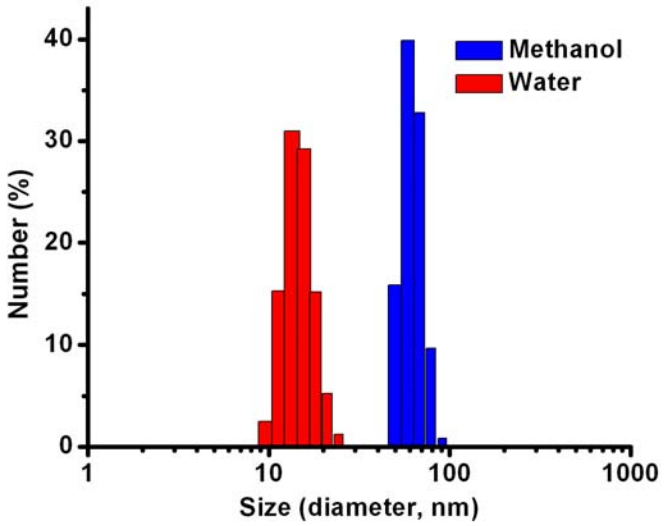

Figure 26. Number distributions of POT_{15}-*b*-PEO_{38} assemblies in methanol and water measured by dynamic light scattering (DLS). The samples were filtered with syringe filters (0.2 μm pore size, Cellulose Acetate filter media) prior to the DLS measurements. Intensity distributions indicated the presence of larger aggregates with multiple peaks at 17 nm, 64 nm, and 370 nm for the water sample and 65 nm and 330 nm for the methanol sample.

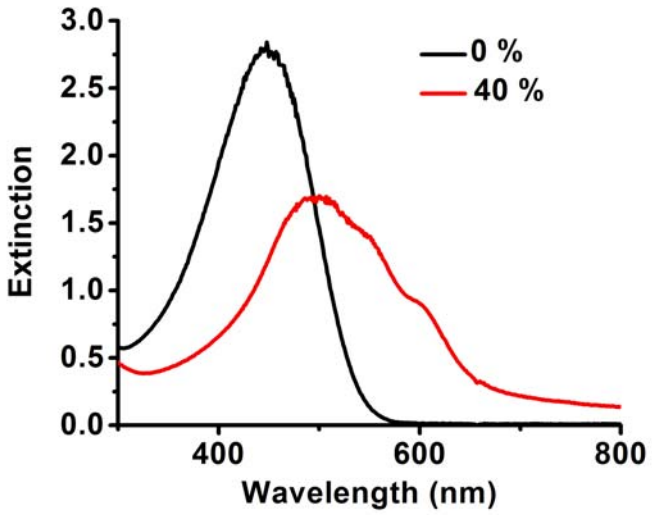

Figure 27. UV/Vis extinction spectra of POT_{15} homopolymers in THF/methanol mixtures at different methanol volume percents.

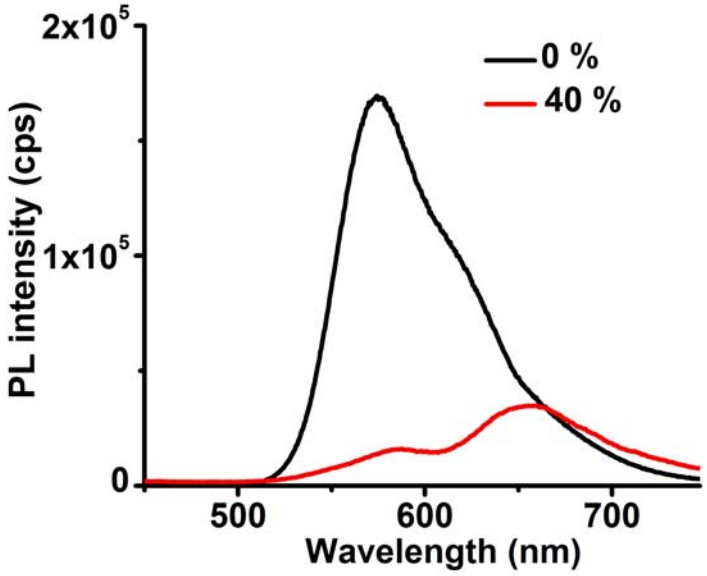

Figure 28. PL spectra of POT_{15} homopolymers in THF/methanol solvent mixtures at different methanol volume percents.

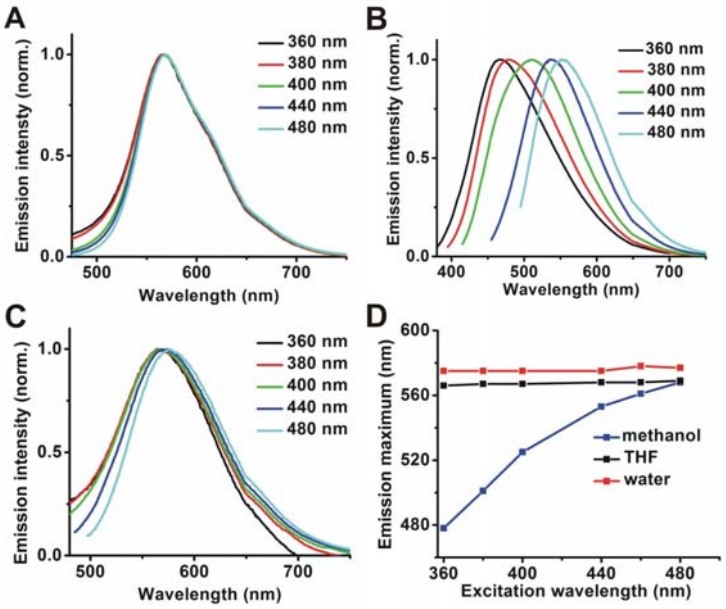

Figure 29. Shifting of emission spectra of POT_{15}-*b*-PEO_{38} in (A) THF, (B) methanol, and (C) water, which were measured at the different excitation wavelengths. (D) Plots showing the change of emission maxima of POT_{15}-*b*-PEO_{38} in methanol, THF, and water.

segment possesses distorted conformation and reduced conjugation lengths in fiber-like assemblies (Figure 23D).

The color changes were completely reversible. As presented in Figure 24B, POT-*b*-PEO showed reversible color changes when they were repeatedly dried and redispersed in different solvents. The reversible emission color changes were also observed by gradually altering the solvent compositions (Figure 24C). These results clearly indicate that the emission property changes are indeed due to the morphological transitions of the block-copolymer assemblies and do not arise as a result of covalent chemical modifications such as photooxidation.

The energy structures in different solvents were more studied through the life time measurements. (Figure 30, Table 2 and 3) Mean lifetimes $<\tau_F>$ of POT_{15}-*b*-PEO_{38} in THF and methanol are comparable to the measured (0.53 ns) and reported lifetimes of poly(3-octylthiophene) (0.52 ns)[32], poly(3-hexylthiophene) (0.51 ns)[39], and poly(3-dodecylthiophene) (0.52 ns)[40] in solution. The measured mean lifetime for both THF and methanol samples (~0.50 ns) can then be attributed to the lifetime of the intrachain exciton, which arises from a transition between π-π* states. Although methanol is a poor solvent for polythiophene, lifetime measurements show that interchain interactions are not significant and only the intrachain exciton affects the fluorescence of POT_{15}-*b*-PEO_{38} in methanol, which explains the high quantum yield relative to that in water. In contrary, strong interchain interactions are evidently present in the water sample from the

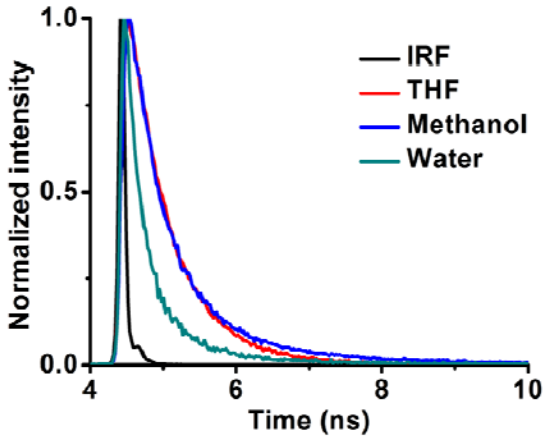

Figure 30. Normalized fluorescence decays of POT_{15}-*b*-PEO_{38} in THF, methanol, and water. (IRF = Instrument response function)

Table 2.

Fluorescence decay parameters of POT and POT-*b*-PEO in various solvents

Sample	Solvent	τ_1[a] (ns)	B_1[b]	τ_2[a] (ns)	B_2[b]	τ_3[a] (ns)	B_3[b]	$\langle\tau_F\rangle$[c]	Fit	χ^2
POT	THF	0.59	0.63	0.42	0.37			0.53	Exponential	1.064
POT	THF	0.53						0.53	Gaussian	1.05
POT-*b*-PEO	THF	0.39	0.54	0.71	0.46			0.54	Exponential	0.926
POT-*b*-PEO	THF	0.53						0.53	Gaussian	0.938
POT-*b*-PEO	H_2O	0.16	0.85	0.73	0.15			0.24	Exponential	0.908
POT-*b*-PEO	MeOH	0.35	0.67	0.83	0.30	2.66	0.03	0.56	Exponential	0.990

[a]Obtained from the reconvolution fit: $A + B_1(\exp(-t/\tau_1) + B_2(\exp(-t/\tau_2)$. [b]Normalized preexponential factor. [c]Amplitude-weighted average lifetime.

Table 3.

Photophysical properties of POT-*b*-PEO in various solvents

Solvent	φ	$\langle\tau_F\rangle$	$k_r\ (ns^{-1})$	$k_{nr}\ (ns^{-1})$	$\tau_r\ (ns)$
THF	0.18 ± 0.01	0.54 ± 0.01	0.34 ± 0.02	1.53 ± 0.03	2.98 ± 0.02
MeOH	0.12 ± 0.01	0.56 ± 0.01	0.21 ± 0.02	1.56 ± 0.02	4.70 ± 0.02
H_2O	0.016 ± 0.003	0.24 ± 0.01	0.07 ± 0.01	4.03 ± 0.02	15.25 ± 0.01
	$\langle\tau_F\rangle = \sum \tau_i B_i$	$k_r = \frac{\phi}{\langle\tau_F\rangle}$	$k_{nr} = \frac{1}{\langle\tau_F\rangle} - k_r$	$\tau_r = \frac{1}{k_r}$	

fast luminescence decay, yielding a mean lifetime of 0.24 ns, which is comparable to data obtained from poly(3-hexylthiophene) films (0.3±0.1 ns)[39]. The resulting radiative lifetime τ_r (15.25 ns) is shorter than 20 ns typical of polythiophene films[40,41], which suggests less packing of polythiophene chains in the block copolymer when dissolved in water. This measurement indicates the different energy profile of POT conjugated backbone in methanol solution and confirms that the fiberlike structures of POT_{15}-*b*-PEO_{38} in methanol are not caused by disordered aggregation by non-solvents, which is shown in conjugated homopolymers and other conjugated block copolymers.

Emission wavelengths of POT-*b*-PEO could be further manipulated by other external stimuli. It is well-known that PEO effectively captures metal ions through ion-dipole interactions.[42] When a potassium iodide solution was added to the methanol solution of POT-*b*-PEO, a gradual blue to green PL color change was observed (Figure 24D), demonstrating a potential use of POT-*b*-PEO as an analytical tool for metal ions.

The emission shifting is highly dependent on type of metal cations. Figure 31A and 31B show red shifting of emission maxima and decrease of emission intensity according to the increased Na^+ concentrations. In the low Na^+ concentration, the emission peak position shows the continuous red-shifting. However, in the high concentration of Na^+, the increase of emission peak positions is leveled-off and it indicates the saturation of the active PEO block to make interaction with the added cations. In a range of concentrations, the emission intensity stops to decrease, increases, and then continues to

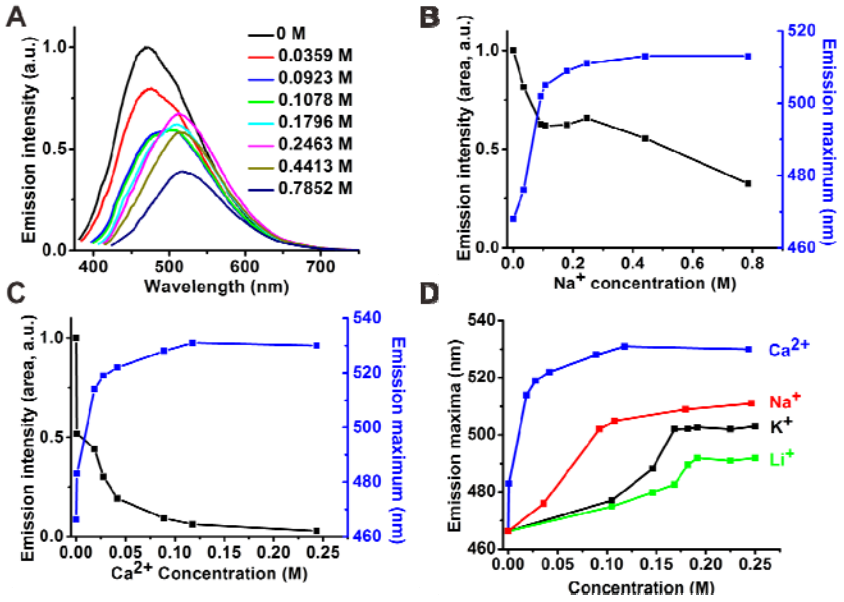

Figure 31. (A) Emission spectra of POT_{15}-*b*-PEO_{38} (9.0×10^{-6} M) : Na^+ in methanol. The concentrations are for those of NaI. (B) and (C) Plots showing the shifting of emission intensity and maxima of POT_{15}-*b*-PEO_{38} : Na^+ and Ca^{2+} in methanol, respectively. (D) Shifting of emission maxima of POT_{15}-*b*-PEO_{38} : metal cations with various concentrations in methanol.

decrease. The pattern reflects the existence of different electronic species with distinct energy profiles. When Ca^{2+} was added instead of Na^{+}, the emission peak positions show the further red shifting and the emission intensities have continuous decrease and finally very low intensity. (Figure 31C and 32) It indicates that Ca^{2+} has higher interaction with PEO and then POT polymer backbone. The ionic size of Ca^{2+} is the almost same as the Na^{+}, but Ca^{2+} prefers 8 coordination with oxygen atoms of PEO backbone, different from 6 coordination of Na^{+}.[43] The higher coordination of Ca^{2+} forms the larger cage and affects further the structures and energy profile of POT backbones. The shifting of emission peak positions of POT_{15}-*b*-PEO_{38} is highly dependent on the type of metal cations. Li^{+} and K^{+} show the less shifting of emission peak positions and the less decrease of emission intensity due to the less interaction with PEO block. This study exhibits the structures and optical properties of POT_{15}-*b*-PEO_{38} dependent on the conformation of PEO block.

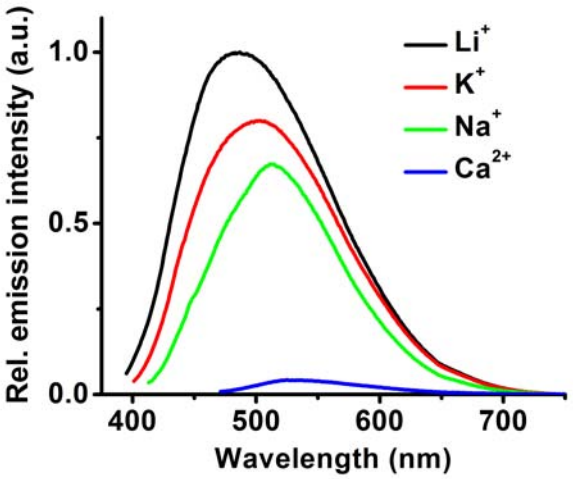

Figure 32. Emission spectra of POT_{15}-*b*-PEO_{38} : metal cations in methanol. The concentrations of metal cations are set to 0.25 M.

4.4.2. POT-*b*-PEO Copolymers with Different Weight Fraction of Each Block

The study using the added cations indicates that PEO block plays a role of determining the structures and optical properties of POT backbone. To check the role of PEO block further, a series of POT-*b*-PEO possessing the same molecular weights of POT block and different molecular weights of PEO block was synthesized using the same synthetic procedures. In THF, all the POT-*b*-PEO shows the similar extinction and emission spectra to confirm the existence as an extended single chain in solution. (Figure 33A and 34A) In methanol the POT_{15}-*b*-PEO_{38} and POT_{15}-*b*-PEO_{42} show the similar pattern of extinction and emission spectra. (Figure 33B and 34B) The spectra are very different from those of POT_{15}-*b*-PEO_{55}, POT_{15}-*b*-PEO_{70}, and POT_{15}-*b*-PEO_{150}. The extinction of longer polymers shows the further red-shifting and the distinct vibronic structures, which are caused by different vibrational energy level of a chain possessing restrict rotation of the conjugated backbone. Also the emission spectra show the further red shifting and lower emission intensity. In water, POT_{15}-*b*-PEO_{38} and POT_{15}-*b*-PEO_{42} exhibit the high scattering factors due to the superstructures of spherical micelles. (Figure 33C) And all the POT-*b*-PEO's show the reduced intensity caused by strong interchain energy transfer of conjugated backbone. This result indicates that the POT-*b*-PEO with a certain range of molecular weight of PEO block behaves differently from the block copolymers with higher molecular weights and PEO block plays a big role of the conformation and energy profile of the POT conjugation backbone in addition to improve

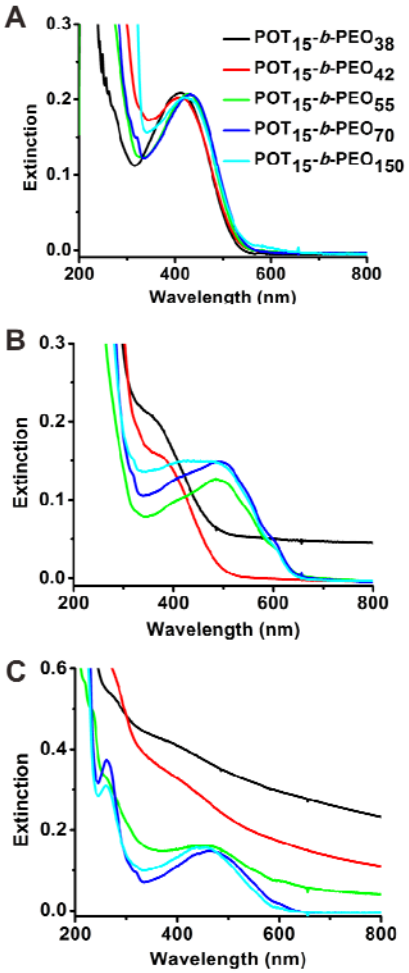

Figure 33. Extinction spectra of POT-*b*-PEO with different molecular weights of PEO in (A) THF, (B) methanol, and (C) water. All the spectra were measured at the concentrations with the same extinction in THF.

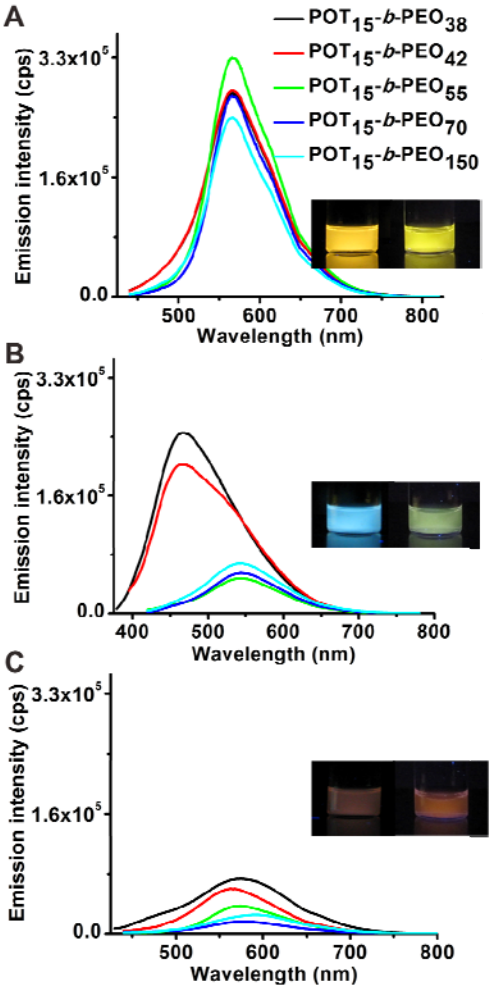

Figure 34. Emission spectra of POT-*b*-PEO with different molecular weights of PEO in (A) THF, (B) methanol, and (C) water. The pictures show the emission colors under UV light. (left: POT_{15}-*b*-PEO_{38}, right: POT_{15}-*b*-PEO_{150}) All the spectra were measured at the concentrations with the same extinction in THF.

the solubility of the conjugated polymers in polar solvents.

The POT-*b*-PEO's with high molecular weights of PEO show different optical response to the added metal cations. (Figure 35A) When Ca^{2+} is added to POT_{15}-*b*-PEO_{150} in methanol, the emission peak positions do not change in contrary to the drastic change of those on POT_{15}-*b*-PEO_{38}. (Figure 35B and 35C) The emission intensities are reduced in the less extent. This result shows that POT_{15}-*b*-PEO_{150} has the different conformation in methanol from POT_{15}-*b*-PEO_{38} and the Ca^{2+} binding with the PEO block does not affect the conformation and energy profile of the POT conjugated backbone.

Figure 36 shows the plausible structural models of POT-*b*-PEO copolymers in water and methanol. POT_{15}-*b*-PEO_{55}, POT_{15}-*b*-PEO_{70}, and POT_{15}-*b*-PEO_{150} exist as the single chains in the both solutions. The steric hindrance of long PEO blocks disrupts the lateral ordering between the POT conjugated backbones and induces the wrapping of POT block to reduce the unfavorable exposure of hydrophobic POT blocks toward polar solvents. At the single molecule level, more planar conformations of POT conjugated backbone are formed and it is evident in appearance of the distinct vibronic structures in the extinction spectra.[44] As the length of PEO block decreases, the POT chains are exposed to polar solvents and in order to exclude the exposure the POT-*b*-PEO should be assembled to some ordered structures such as spherical micelle, at which POT blocks are placed at inside core and PEO blocks are stretched out. Dynamic light scattering (DLS)

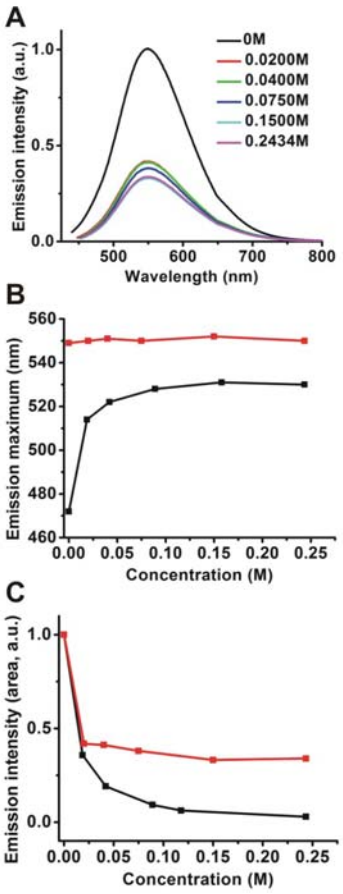

Figure 35. (A) Emission spectra of POT_{15}-*b*-PEO_{150} (9.0×10^{-6} M) : Ca^{2+} in methanol. The concentrations are for those of CaI_2. (B) and (C) Plots showing the shifting of emission maximum and intensity of POT_{15}-*b*-PEO_{38} : Ca^{2+} (black) and POT_{15}-*b*-PEO_{150} : Ca^{2+} (red) in methanol, respectively.

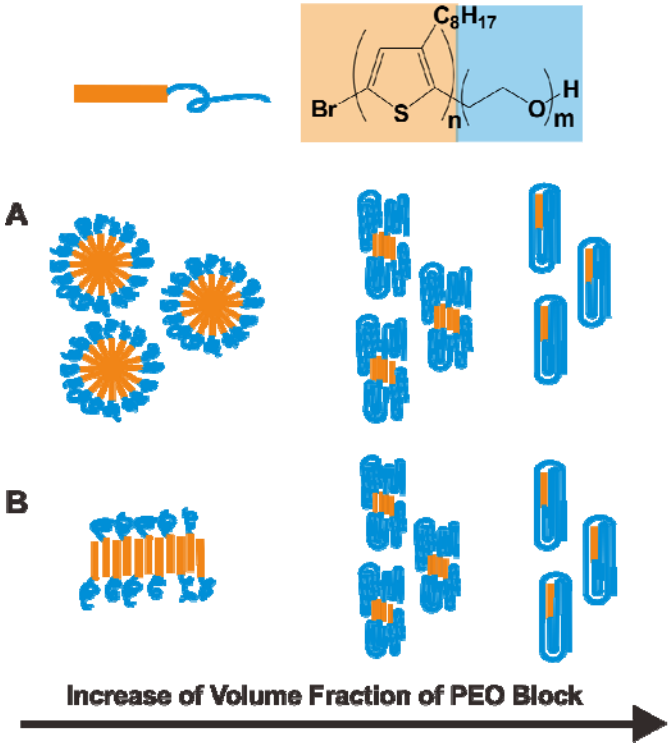

Figure 36. Structural models showing different conformations of POT-*b*-PEO in (A) water and (B) methanol.

experiments in water and methanol show the consistent results to the models. (Table 4) However, the POT-*b*-PEO with the lower molecular weight of PEO such as POT_{15}-*b*-PEO_{38} and POT_{15}-*b*-PEO_{42} forms the distinct structures in water and methanol. High polarity of water induces the tightly-packed spherical micellar conformation to show the red-shifting of extinction and emission and the low emission intensity due to dominant interchain energy transfer. In methanol the hydrodynamic volume of PEO becomes smaller and the lateral ordering of between the POT backbones becomes dominant to form the fiber-like structures with the less contact area toward the methanol. In the fiber-like structures the steric effect caused by hydrodynamic volume of PEO block disrupts the energy migration through the conjugation backbone to induce the blue shifting of extinction and emission spectra. The various supramolecular structures formed by POT-*b*-PEO apparently reflect a delicate balance of interactions between the POT and PEO blocks that is sensitive to polymer composition.

Table 4. Number distribution of POT-*b*-PEO in methanol and water measured by dynamic light scattering (DLS).

	Solvent	Diameter (nm)	PDI	
POT_{15}-*b*-PEO_{38}	CH_3OH	65.7	0.341	assembly
POT_{15}-*b*-PEO_{38}	H_2O	15.1	0.495	assembly
POT_{15}-*b*-PEO_{42}	CH_3OH	78.1	0.379	assembly
POT_{15}-*b*-PEO_{42}	H_2O	40.9	0.222	assembly
POT_{15}-*b*-PEO_{55}	CH_3OH	47.5	0.261	assembly
POT_{15}-*b*-PEO_{55}	H_2O	29.4	0.265	assembly
POT_{15}-*b*-PEO_{70}	CH_3OH	5.38	0.182	single chain
POT_{15}-*b*-PEO_{70}	H_2O	8.07	0.301	single chain
POT_{15}-*b*-PEO_{150}	CH_3OH	6.20	0.342	single chain
POT_{15}-*b*-PEO_{150}	H_2O	3.27	0.323	single chain

4.5. Conclusion

This section has shown a versatile way to manipulate the light emission properties of conjugated polymers through the precise control of their assembly structure based on the block copolymer approach. A series of amphiphilic POT-*b*-PEO copolymers with different PEO block lengths was synthesized and their optical properties dependent on their structures in solution were studied. The POT-*b*-PEO forms the distinct supramolecular structures in response to the external environment such as solvent polarity and added metal cations, which affect the optical properties through the distortion of POT conjugation backbone. The PEO blocks play a big role to form the supramolecular structure and determine the optical properties as well as to enhance the solubility in polar solvents.

Supramolecular self-assembly has been extensively explored for the past decade as a way to tune the properties of molecule-based materials. However, much of the research has been focused on making complex molecular architectures rather than utilizing the correlation between the structure and properties. This study described here demonstrates that a wide range of PL colors can be obtained without altering the molecular structure, clearly demonstrating that self-assembly can be used as a way to manipulate materials properties in a highly controllable fashion. In addition, this result shows that POT-*b*-PEO should be one of proper materials to study the correlation

between the structures and the optical properties because the structure could be easily controlled by the minuscule change of environment and it affects the optical properties to facilitate the easy measurement. Also the strategy to use the conjugated block copolymers would be an efficient strategy to tune the material properties in a predetermined way.

4.7. Reference

(1) Friend, R. H.; Gymer, R. W.; Holmes, A. B.; Burroughes, J. H.; Marks, R. N.; Taliani, C.; Bradley, D. D. C.; Dos Santos, D. A.; Bredas, J. L.; Logdlund, M.; Salaneck, W. R. *Nature* **1999**, *397*, 121.

(2) Heeger, A. J. *Angew. Chem., Int. Ed.* **2001**, *40*, 2591.

(3) Li, G.; Shrotriya, V.; Huang, J. S.; Yao, Y.; Moriarty, T.; Emery, K.; Yang, Y. *Nature Mater.* **2005**, *4*, 864.

(4) Dias, F. B.; King, S.; Monkman, A. P.; Perepichka, II; Kryuchkov, M. A.; Perepichka, I. F.; Bryce, M. R. *J. Phys. Chem. B* **2008**, *112*, 6557.

(5) Olsen, B. D.; Segalman, R. A. *Mater. Sci. Eng., R* **2008**, *62*, 37.

(6) Yang, H. H.; LeFevre, S. W.; Ryu, C. Y.; Bao, Z. N. *Appl. Phys. Lett.* **2007**, *90*.

(7) Segalman, R. A.; McCulloch, B.; Kirmayer, S.; Urban, J. J. *Macromolecules* **2009**, *42*, 9205.

(8) Perepichka, I. F.; Perepichka, D. F.; Meng, H.; Wudl, F. *Adv. Mater.* **2005**, *17*, 2281.

(9) Jenekhe, S. A.; Chen, X. L. *Science* **1998**, *279*, 1903.

(10) Wang, H. B.; Wang, H. H.; Urban, V. S.; Littrell, K. C.; Thiyagarajan, P.; Yu, L. P. *J. Am. Chem. Soc.* **2000**, *122*, 6855.

(11) Hulvat, J. F.; Sofos, M.; Tajima, K.; Stupp, S. I. *J. Am. Chem. Soc.* **2005**, *127*, 366.

(12) Richard, F.; Brochon, C.; Leclerc, N.; Eckhardt, D.; Heiser, T.; Hadziioannou, G. *Macromol. Rapid Commun.* **2008**, *29*, 885.

(13) Sivula, K.; Ball, Z. T.; Watanabe, N.; Frechet, J. M. J. *Adv. Mater.* **2006**, *18*, 206.

(14) Liu, J. S.; Sheina, E.; Kowalewski, T.; McCullough, R. D. *Angew. Chem., Int. Ed.* **2002**, *41*, 329.

(15) Boudouris, B. W.; Frisbie, C. D.; Hillmyer, M. A. *Macromolecules* **2008**, *41*, 67.

(16) Dai, C. A.; Yen, W. C.; Lee, Y. H.; Ho, C. C.; Su, W. F. *J. Am. Chem. Soc.* **2007**, *129*, 11036.

(17) Leclere, P.; Surin, M.; Viville, P.; Lazzaroni, R.; Kilbinger, A. F. M.; Henze, O.; Feast, W. J.; Cavallini, M.; Biscarini, F.; Schenning, A. P. H. J.; Meijer, E. W. *Chem. Mater.* **2004**, *16*, 4452.

(18) Roncali, J. *J. Mater. Chem.* **1999**, *9*, 1875.

(19) Yamamoto, Y.; Sanechika, K.; Yamamoto, A. *J. Polym. Sci., Polym. Lett. Ed.* **1980**, *18*, 9.

(20) Yoshino, K.; Hayashi, S.; Sugimoto, R. *Jpn. J. Appl. Phys., Part 2* **1984**, *23*, L899.

(21) McCullough, R. D.; Lowe, R. D. *J. Chem. Soc., Chem. Commun.* **1992**, 70.

(22) Loewe, R. S.; Khersonsky, S. M.; McCullough, R. D. *Adv. Mater.* **1999**, *11*, 250.

(23) Chen, T. A.; Rieke, R. D. *J. Am. Chem. Soc.* **1992**, *114*, 10087.

(24) McCullough, R. D.; Ewbank, P. C.; Loewe, R. S. *J. Am. Chem. Soc.* **1997**, *119*, 633.

(25) Guillerez, S.; Bidan, G. *Synth. Met.* **1998**, *93*, 123.

(26) McCullough, R. D.; Tristram-Nagle, S.; Williams, S. P.; Lowe, R. D.; Jayaraman, M. *J. Am. Chem. Soc.* **1993**, *115*, 4910.

(27) Klok, H. A.; Lecommandoux, S. *Adv. Mater.* **2001**, *13*, 1217.

(28) Kuo, C.-C.; Tung, Y.-C.; Lin, C.-H.; Chen, W.-C. *Macromol. Rapid Commun.* **2008**, *29*, 1711.

(29) Li, C.; Hsu, J.-C.; Sugiyama, K.; Hirao, A.; Chen, W.-C.; Mezzenga, R. *Macromolecules* **2009**, *42*, 5793.

(30) Wang, H.; Wang, H. H.; Urban, V. S.; Littrell, K. C.; Thiyagarajan, P.; Yu, L. *J. Am. Chem. Soc.* **2000**, *122*, 6855.

(31) Olsen, B. D.; Segalman, R. A. *Macromolecules* **2005**, *38*, 10127.

(32) Theander, M.; Inganas, O.; Mammo, W.; Olinga, T.; Svensson, M.; Andersson, M. R. *J. Phys. Chem. B* **1999**, *103*, 7771.

(33) Jeffries-El, M.; Sauve, G.; McCullough, R. D. *Macromolecules* **2005**, *38*, 10346.

(34) Iovu, M. C.; Jeffries-El, M.; Sheina, E. E.; Cooper, J. R.; McCullough, R. D. *Polymer* **2005**, *46*, 8582.

(35) Sung, J. H.; Lee, D. C.; Park, H. J. *Polymer* **2007**, *48*, 4205.

(36) Grey, J. K.; Kim, D. Y.; Norris, B. C.; Miller, W. L.; Barbara, P. F. *J. Phys. Chem. B* **2006**, *110*, 25568.

(37) Tu, G. L.; Li, H. B.; Forster, M.; Heiderhoff, R.; Balk, L. J.; Sigel, R.; Scherf, U. *Small* **2007**, *3*, 1001.

(38) Inganas, O.; Salaneck, W. R.; Osterholm, J. E.; Laakso, J. *Synth. Met.* **1988**, *22*, 395.

(39) Magnani, L.; Rumbles, G.; Samuel, I. D. W.; Murray, K.; Moratti, S. C.; Holmes, A. B.; Friend, R. H. *Synth. Met.* **1997**, *84*, 899.

(40) Rumbles, G.; Samuel, I. D. W.; Magnani, L.; Murray, K. A.; DeMello, A. J.; Crystall, B.; Moratti, S. C.; Stone, B. M.; Holmes, A. B.; Friend, R. H. *Synth. Met.* **1996**, *76*, 47.

(41) Ruseckas, A.; Namdas, E. B.; Theander, M.; Svensson, M.; Yartsev, A.; Zigmantas, D.; Andersson, M. R.; Inganas, O.; Sundstrom, V. *J. Photochem. Photobiol. A-Chem.* **2001**, *144*, 3.

(42) Quina, F.; Sepulveda, L.; Sartori, R.; Abuin, E. B.; Pino, C. G.; Lissi, E. A. *Macromolecules* **1986**, *19*, 990.

(43) Crawford, K. B.; Goldfinger, M. B.; Swager, T. M. *J. Am. Chem. Soc.* **1998**, *120*, 5187.

(44) Kiriy, N.; Jahne, E.; Adler, H. J.; Schneider, M.; Kiriy, A.; Gorodyska, G.; Minko, S.; Jehnichen, D.; Simon, P.; Fokin, A. A.; Stamm, M. *Nano Lett.* **2003**, *3*, 707.

Part IV:

Self-Assembly of Conjugated Polymers and Nanomaterials

5.1. Introduction

Polymer-nanomaterial composites have attracted considerable attention in recent years because the intimate combination of polymer and nanomaterials offers the promise of interesting properties that are not possible from each component alone. Especially the hybrid materials consisting of conjugated polymers have emerged as an important class of materials for a range of applications including photovoltaic solar cells and biological sensing, owing to their unique optical and electrical properties and processibility.[1-5] Because the properties and device performances depend highly on the interface and location of each active component, it is important to develop effective ways to control the nanoscale architectures of the hybrid materials both for their technological applications and fundamental studies.

This section shows that amphiphilic conjugated block copolymers consisting of poly(3-octylthiophene) (POT) and poly(ethylene oxide) (PEO) were used for the dispersion of SWNTs and form the stable dispersion with SWNTs in aqueous solution. POT blocks form the strong interaction with the wall of SWNTs and PEO blocks, which were stretched out from the surface, provide the aqueous solubility and biocompatibility

to the de-bundled SWNTs. In addition, this section describes that the POT-*b*-PEO copolymers can act as a template to induce the heterogeneous nanostructures as well as an active component of novel multifunctional nanostructures.

5.2. POT-*b*-PEO : Carbon Nanotube Hybrid Nanostructures

5.2.1. Introduction

Since the discovery of carbon nanotubes (CNTs) there have been numerous reports about the formation of stable dispersion of CNTs[6] because the bundled CNTs form strong interaction between nanotubes and show poor solubility which limits the various applications.[7] Of various CNT dispersion methods the use of dispersant has recently attracted much interest.[8] The dispersants including surfactant, block copolymers, and biomaterials form non-covalent interaction between dispersant and CNT, which does not interrupt the conjugation of nanotube but preserves the electrical and optical properties of intrinsic CNT in the dispersion.

Especially, conjugated polymers containing aromatic rings form the strong interaction with the carbon nanotube surface via π-π non-covalent bonding and stabilize the de-bundled carbon nanotubes against van der Waals interaction between nanotubes.[9] Also conjugated polymers possess unique optical and electrical properties and the composite materials consisting of the conjugated polymers and SWNTs are expected to produce novel and enhanced optoelectronic effects.[10]

Poly(phenylacetylene) was the first conjugated polymer that was mixed with CNT.[11] The composite was prepared by in situ polymerization of phenylacetylene in the presence of the CNTs. The polymer chain wraps the CNTs helically and solubilizes the blend in organic solvents. Under harsh laser irradiation, the nanotubes exhibited a strong photostabilization effect, protecting the wrapped polymer from photodegradation.

Due to the great promise of conjugated polymer composites in optoelectronic application, the CNT composites with poly(phenylenevinylene) (PPV) and the derivatives has been studied extensively. The CNT was mixed with PPV and their optical properties were investigated. The quantum efficiency obtained was 1.8 %,[12] which arises mainly from the complex interpenetrating network of polymer chains with the nanotube film. The predominant electronic interaction between the two components is nonradiative energy transfer from the excited polymer to the tubes.

A polymer that has been studied extensively in optoelectronic applications as a CNT dopant is poly(*m*-phenylene vinylene-*co*-2,5-dioctyloxy-*p*-phenylene vinylene) (PmPV). The substitution pattern of the polymer chain leads to dihedral angles resulting in a helical structure. The coiled conformation allows the polymer to surround the surface of nanotubes by interacting with π-π forces. After the incorporation of CNT, the electrical conductivity of the conjugated polymer film was increased by up to 8 orders of magnitude.[13]

In a recent work, Therien and co-workers used amphiphilic, linear conjugated

poly(*p*-phenyleneethynylene) as a dispersant of SWNTs and exhibited the helically wrapped SWNT supramolecular structures by polymer monolayer.[14] The observed polymer pitch length confirmed structural predictions made via molecular dynamics simulations.

Notably the conjugated polymer comprising the backbone of 9, 9-dialkyl-2, 7-fluorene subunits displayed the selective dispersion for semiconducting CNTs. Furthermore, mainly semiconducting tubes with differences in indices (*n*-*m*) = 1 or 2 and thus large chiral angles were dispersed by these polymers. Variation of the polymer backbone by different aryl subunits interlinking the fluorenes enabled further fine-tuning of the observed selectivities.[15]

Other family of materials with potential for CNT dispersant is block copolymer. One block of the polymer forms a close interaction with the carbon nanotube walls, while the other block provides the solubility to the de-bundled nanotubes by forming a steric barrier or repulsion interaction between polymer-wrapped nanotubes. Due to the strong interaction between conjugated polymers and carbon nanotubes conjugated block copolymers with a conjugated polymer block and a non-conjugated polymer block should be an good dispersant for carbon nanotube dispersion/stabilization. The conjugated polymer block can form strong π-π interactions with carbon nanotube walls, while the non-conjugated polymer block will provide the de-bundled CNTs with a good solubility and stability in a wide range of solvents and host polymer matrices. In a recent work, Zou

et al. showed that the block copolymer containing conjugated polymer block acts as an good dispersant of carbon nanotubes.[16]

In this section, amphiphilic conjugated block copolymer POT-*b*-PEO consisting of POT as a conjugated polymer block and PEO as a non-conjugated block was used to produce the stable dispersion of carbon nanotubes in aqueous solution. (Scheme 6) Furthermore, the non-conjugated blocks possess the functional groups to be used for further modification and application. Especially, PEO as a non-conjugated block shows the strong interaction with the metal cations and would be useful to template the synthesis of the new types of hybrid nanomaterials. Also PEO is known to be biocompatible and possesses a functional group for attachment of biomolecules.

5.2.2. Experimental Section

POT-*b*-PEO was synthesized by a reported procedure[17] and POT_{15}-*b*-PEO_{38} and POT_{15}-*b*-PEO_{150} having different molecular weights were used for the SWNT dispersion experiment. For the synthesis of longer POT_{15}-*b*-PEO_{150}, more amounts (15 mL) of ethylene oxide were added and the longer polymerization reaction time (4 days) was allowed. The molecular weight was estimated to be *M*n = 4700 and 8900 g/mol using ^{1}H NMR end-group analysis and the polydispersity indices (PDI) were measured to be 1.45 and 1.10 using gel permeation chromatography (GPC). SWNT (SWeNT® SG 65) was purchased from Aldrich with a diameter of 0.7 ~ 0.9 nm and a purity above 90 %. All other reagents were purchased from Aldrich.

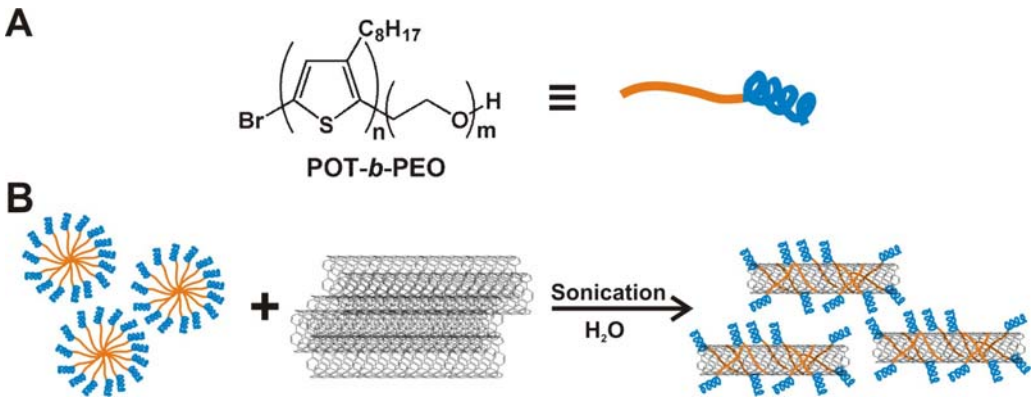

Scheme 6. (A) Chemical structure of POT-*b*-PEO and (B) schematic description of SWNT dispersed by POT-*b*-PEO in water. Orange line and blue coil represent the POT and PEO blocks of the block copolymers, respectively.

All the dispersion experiments were carried out by the following procedure unless otherwise noted. The as-received SWNTs were sonicated in chloroform (0.5 mg/mL) and used as a stock solution. 1 mL of the stock solution was completely dried and the dried SWNTs were mixed with POT_{15}-*b*-PEO_{38} (4 mg) in water (2 mL). The mixture was sonicated for 1 hr and centrifuged at 2000 rpm for 10 min to remove the undispersed SWNTs. 200 μL of the upper supernatant were transferred to a vial and diluted to 1 mL to measure UV-NIR and photoluminescence measurement.

For the synthesis of SWNT/POT-*b*-PEO/Au hybrid materials, 10 μL of $HAuCl_4$ in water (1.0 wt. %) were added to 200 μL solution of the as-purified SWNT/ POT_{15}-*b*-PEO_{38}. The mixture was heated in the oil bath (90^{o}C) for 1 hr and cooled down to room temperature. Transmission electron microscopy (TEM) was performed on a JEOL TEM-2010F operating at 200 kV accelerating voltage. Vis-NIR extinction measurement was conducted by Agilent 8453 UV-vis spectroscopy system. Photoluminescence measurements were recorded with a Fluorolog®-3 spectrofluorometer (HORIBA Jobin Yvon, Inc.) utilizing an R928 PMT detector.

5.2.3. Result and Discussion

By mild sonication, SWNTs were well dispersed in aqueous solution and the solution was stable for several months without showing the noticeable precipitation

irrespective of molecular weight of POT-*b*-PEO. (Figure 37A) Figure 37B shows a representative TEM image of the dispersion and the SWNTs in the solution mostly exist as the individual tubes or small bundles consisting of a few tubes. To examine the deposition of POT_{15}-*b*-PEO_{38} on the carbon nanotube wall, the TEM grid was stained by osmium tetroxide (OsO_4). The TEM image (Figure 37C) shows the dark contrast on the carbon nanotube surface. Because OsO_4 selectively stains the PEO segment of the block copolymer,[18] this demonstrates the existence of a layer consisting of block copolymers on the carbon nanotube surface.

Extinction spectroscopy shows the existence of the characteristic (6, 5) and (7, 6) SWNTs. (Figure 38A) The well-resolved extinction peaks indicate that the dispersion exists as individually de-bundled carbon nanotubes.[19] The interaction between POT_{15}-*b*-PEO_{38} and SWNT was studied by photoluminescence (PL) spectroscopy. Figure 38B shows the strong quenching of the SWNT/ POT_{15}-*b*-PEO_{38} dispersion in aqueous solution due to electron/energy transfer[5] and this result indicates the strong interaction between POT-*b*-PEO and SWNT.

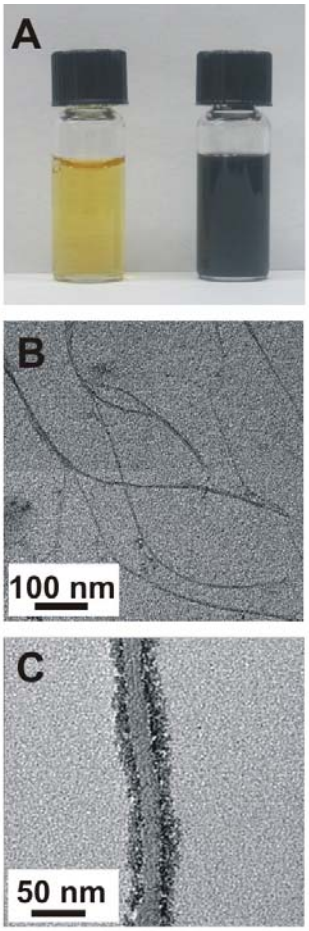

Figure 37. (A) Pictures of POT_{15}-*b*-PEO_{38} (left) and POT_{15}-*b*-PEO_{38} / SWNT dispersion (right) in aqueous solution. TEM images of POT_{15}-*b*-PEO_{38} / SWNT dispersion (B) without and (C) with OsO_4 staining.

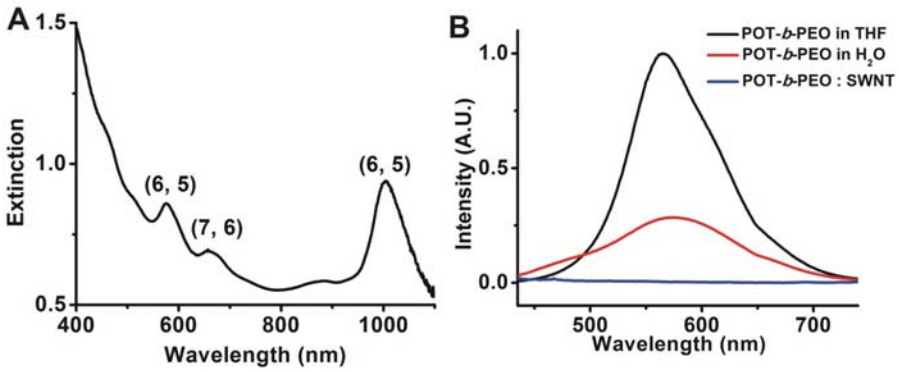

Figure 38. (A) Vis-NIR extinction spectra of POT_{15}-*b*-PEO_{38}/SWNT dispersion in aqueous solution. (B) Photoluminescent (PL) spectra of POT_{15}-*b*-PEO_{38} in THF and water and POT_{15}-*b*-PEO_{38}/SWNT dispersion in aqueous solution. All the samples were excited at 400 nm.

The extent of SWNT dispersion by POT-*b*-PEO was estimated by using POT_{15}-*b*-PEO_{38}, POT_{15}-*b*-PEO_{150}, and sodium dodecylsulfate (SDS). POT_{15}-*b*-PEO_{150} exhibits the higher extinction of SWNT dispersion than POT_{15}-*b*-PEO_{38} (Figure 39A) and the higher extinction is caused by higher concentration of SWNT in solution. This result demonstrates that PEO acts as a steric barrier to prevent the de-bundled SWNTs from forming aggregation and for the purpose the longer PEO segments are more efficient due to higher steric effect. Figure 39B shows the higher extinction and more dispersion could be made by higher concentration of POT-*b*-PEO. It indicates that dispersion of SWNTs is just caused by POT-*b*-PEO. When the same mass of SDS was used as a dispersant, the extinction is much lower than that of POT_{15}-*b*-PEO_{150} (Figure 39C), showing that POT-*b*-PEO is a better dispersant than SDS.

PEO has the strong interaction with other species such as metal cations and the dispersed SWNT/POT-*b*-PEO can be used to template novel nanostructures. When $HAuCl_4$ was added to the as-dispersed SWNT/POT-*b*-PEO, the Au cations were reduced and form the Au nanoparticles by heating. Interestingly, the formed Au nanoparticles were assembled to form bigger superstructures. (Figure 40A) All the superstructures were connected by SWNT strands and it indicates that SWNT/POT-*b*-PEO affects the formation of the structures strongly. Figure 40B shows that the superstructures consist of small Au nanoparticles. As a plausible mechanism, the SWNT facilitates the reduction of

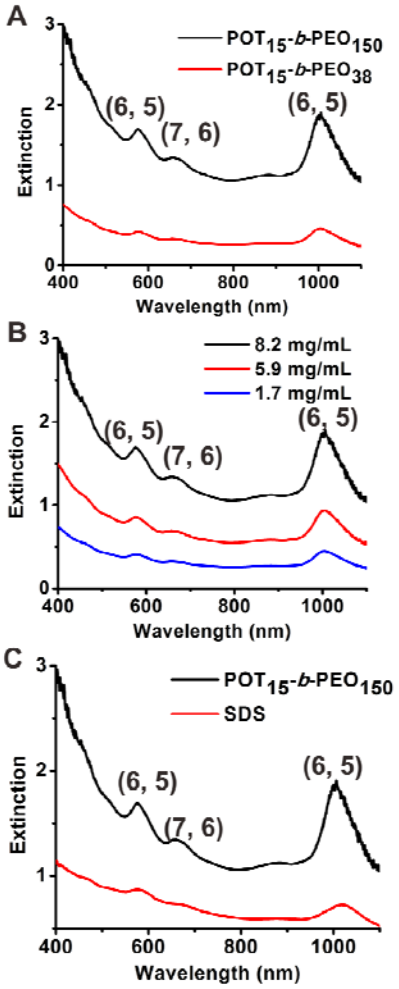

Figure 39. Vis-NIR extinction spectra of SWNT dispersion in aqueous solution by (A) the same mass concentration (8.2 mg/mL) of POT_{15}-*b*-PEO_{38} and POT_{15}-*b*-PEO_{150}, (B) different concentrations of POT_{15}-*b*-PEO_{150}, and (C) the same mass concentration (8.2 mg/mL) of SDS and POT_{15}-*b*-PEO_{150}. All the experiments were carried out by using the same weight of SWNTs (1.1 mg) in 1 mL of aqueous solution of POT-*b*-PEO or SDS. All the samples were diluted by 5 times prior to Vis-NIR measurement.

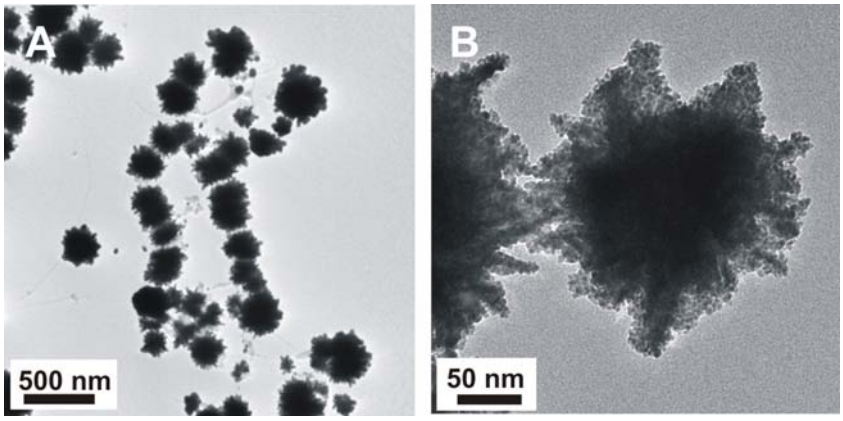

Figure 40. TEM images of SWNT/ POT_{15}-*b*-PEO_{38}/Au hybrid nanostructures in (A) low and (B) high magnification.

gold cations and the reduced gold atoms start to grow gold nanoparticles. PEOs on the wall of SWNTs have strong interaction with the formed Au nanoparticles and produce the aggregated superstructures. The hybrid nanostructures would be used for many applications including electronic devices and biological conjugation.

5.3. POT-*b*-PEO : Metal Hybrid Nanostructures

5.3.1. Introduction

Increasing attention has been paid to colloidal nanoparticles with a discrete shape, structure, and composition because they have great promise for optical, electronic, and sensory application. In recent years many methods[20-23] have been reported for generating polymeric shells around inorganic nanoparticles because the intimate combination of polymeric and inorganic components can offer interesting properties that are not possible from either metal alone. The synthetic methods of inorganic-polymeric hybrid colloidal particle could be demonstrated into a facile, robust procedure for the preparation of colloidal nanoparticles with the desired structures. This section shows that POT-*b*-PEO acts as a template as well as a polymeric component to produce a discrete polymer : metal hybrid nanostructure.

5.3.2. Experimental Section

The POT-*b*-PEO : metal hybrid nanoparticles were synthesized using gold or silver

metals and POT-*b*-PEO copolymers. The hybrid nanoparticles have the distinctive architectures dependent on the interaction between metal ions and conjugated block copolymers. In a typical synthesis, 200 μL of POT_{15}-*b*-PEO_{38} copolymer (1.0 mg/mL) and 10 μL of $HAuCl_4$ (w/w 1 %) or 20 μL of $AgNO_3$ (0.02 M) aqueous solutions were added into the flask with stirring. After 5 min, a reducing agent NH_2OH (20 mM, 20 μL) was introduced to initiate the gold or silver nanoparticle growth. The solution then changed from light yellow to purple (gold) or milky grey color (silver) over 1 hour, indicating formation of gold or silver nanoparticles.

5.3.3. Result and Discussion

Figure 41A shows representative transmission electron microscopy (TEM) images of POT-*b*-PEO : Au hybrid nanoparticles. The diameters of each nanoparticles are estimated to ~ 200 nm and all the particles are uniform and consist of many small particles, which show the lattice fringes indicating their crystallinity (Figure 42). Also the UV/vis extinction spectra (Figure 41B) taken from the solution that used for electron microscopy exhibit the distinctive surface plasmon resonance peak from gold nanoparticles. To elucidate a role of POT-*b*-PEO copolymer, a control experiment was executed with the same procedure using poly(ethylene glycol) methyl ether (MPEG) instead of POT-*b*-PEO copolymer. The TEM image (Figure 43) shows the big aggregation with irregular size and shape were formed and it indicates that POT segments

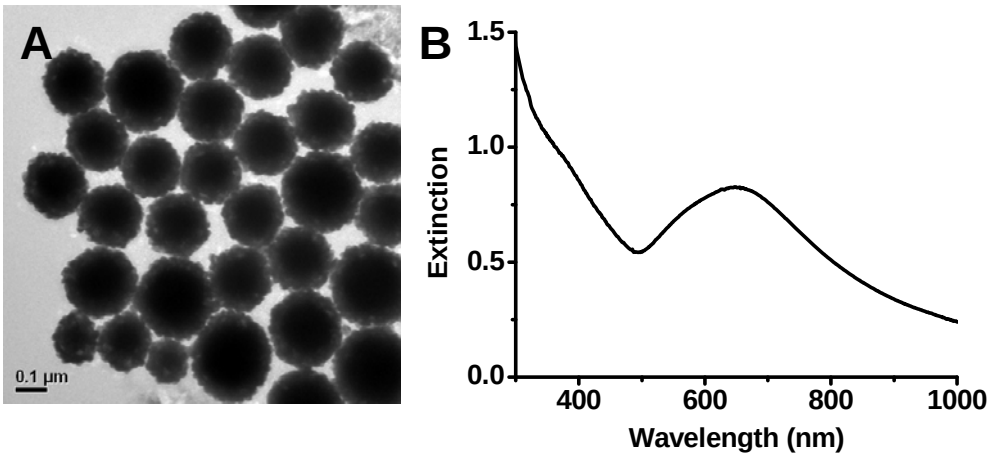

Figure 41. (A) TEM images and (B) UV-vis extinction of POT-*b*-PEO : Au hybrid nanoparticles.

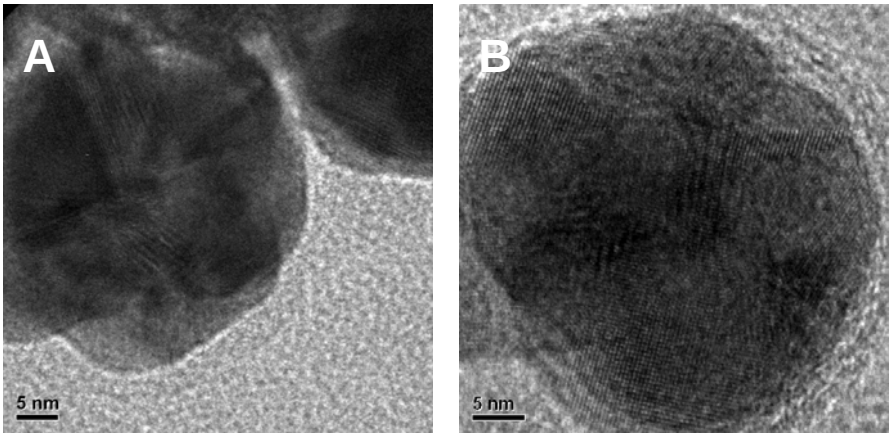

Figure 42. HRTEM images of (A) POT-*b*-PEO : Au and (B) POT-*b*-PEO : Ag hybrid nanoparticles.

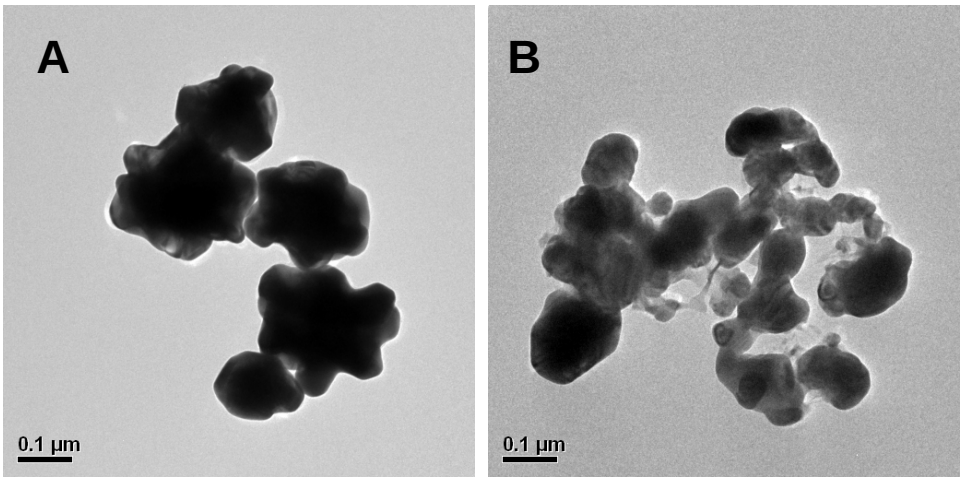

Figure 43. TEM images of (A) MPEG : Au and (B) MPEG : Ag nanoparticles.

in POT-*b*-PEO copolymer play a big role in forming the uniform superstructures of the POT-*b*-PEO : Au hybrids.

When silver ions were used rather than gold ions to fabricate the hybrid nanostructures, the formed POT-*b*-PEO : Ag hybrid nanoparticles interestingly have anisotropic nanoarchitectures, which consist of two segments showing bright and dark contrast. (Figure 44) The segments with dark contrast show the lattice fringes reflecting the crystallinity (Figure 42B), but other segment with bright contrast does not possess the crystallinity indicating the amorphous structure. It demonstrates that the nanoparticles have distinctive nanoarchitectures with anisotropy. One segment consists of inorganic silver nanoparticles and the other does organic POT-*b*-PEO copolymers. Also the UV/vis extinction spectra (Figure 44B) exhibit the distinctive surface plasmon resonance peak from silver nanoparticles. On the contrary, the control experiment using MPEG instead of the POT-*b*-PEO copolymer shows just big aggregations without specific shape and size (Figure 43B), indicating that POT segments play the big role in forming the anisotroic nanostructures.

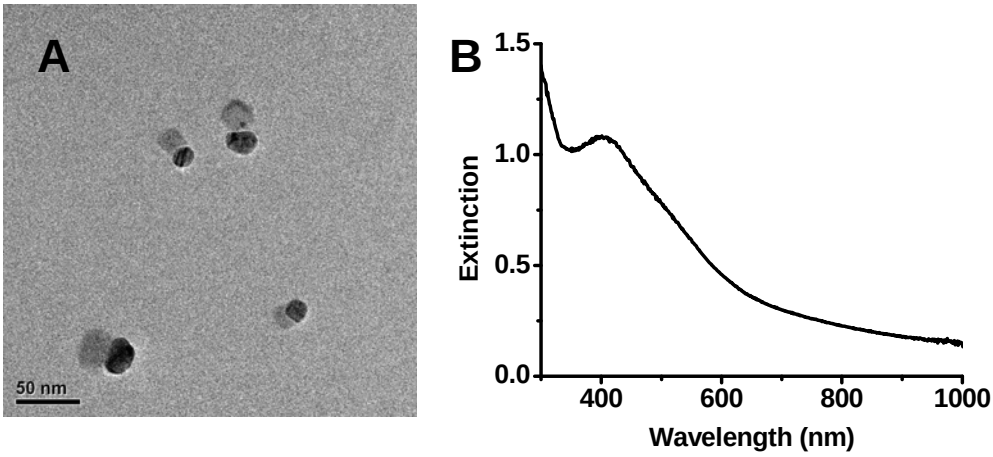

Figure 44. (A) TEM image and (B) UV-vis extinction of POT-*b*-PEO : Ag hybrid nanoparticles

5.4. Conclusion

SWNTs are dispersed in aqueous solution by using amphiphilic conjugated block copolymer as a dispersant. The dispersion is stable due to the strong π-π non-covalent interaction between the conjugated backbone of POT segments and the wall of SWNTs and steric effect of PEO segments. The SWNT/POT-*b*-PEO can be used for a template to produce novel nanomaterials with different shapes and properties.

In addition, this work describes a facile way to generate metal-polymer hybrid nanostructures. The conjugated POT-*b*-PEO copolymers act as a structure-directing template to manipulate the geometrical development and particle conformation of gold and silver nanoparticles. This procedure should be applicable to many different types of metal nanoparticles and furthermore these hybrid particles are expected to find applications as a new class of materials of optoelectronic device and biological sensing.

5.5. Reference

(1) Lu, X.; Zhang, W.; Wang, C.; Wen, T.-C.; Wei, Y. *Prog. Polym. Sci* **2011**, *36*, 671.

(2) Dayal, S.; Kopidakis, N.; Olson, D. C.; Ginley, D. S.; Rumbles, G. *J. Am. Chem. Soc.* **2009**, *131*, 17726.

(3) Liao, H.-C.; Chen, S.-Y.; Liu, D.-M. *Macromolecules* **2009**, *42*, 6558.

(4) Stavrinadis, A.; Beal, R.; Smith, J. M.; Assender, H. E.; Watt, A. A. R. *Adv. Mater.* **2008**, *20*, 3105.

(5) Fan, C. H.; Wang, S.; Hong, J. W.; Bazan, G. C.; Plaxco, K. W.; Heeger, A. J. *Proc. Natl. Acad. Sci. U. S. A.* **2003**, *100*, 6297.

(6) Grossiord, N.; Loos, J.; Regev, O.; Koning, C. E. *Chem. Mat.* **2006**, *18*, 1089.

(7) Girifalco, L. A.; Hodak, M.; Lee, R. S. *Phys. Rev. B* **2000**, *62*, 13104.

(8) Tasis, D.; Tagmatarchis, N.; Bianco, A.; Prato, M. *Chem. Rev.* **2006**, *106*, 1105.

(9) Yang, M. J.; Koutsos, V.; Zaiser, M. *J. Phys. Chem. B* **2005**, *109*, 10009.

(10) Heeger, A. J. *Angew. Chem.-Int. Edit.* **2001**, *40*, 2591.

(11) Tang, B. Z.; Xu, H. *Macromolecules* **1999**, *32*, 2569.

(12) Ago, H.; Petritsch, K.; Shaffer, M. S. P.; Windle, A. H.; Friend, R. H. *Adv. Mater.* **1999**, *11*, 1281.

(13) Star, A.; Lu, Y.; Bradley, K.; Grüner, G. *Nano Lett.* **2004**, *4*, 1587.

(14) Kang, Y. K.; Lee, O. S.; Deria, P.; Kim, S. H.; Park, T. H.; Bonnell, D. A.; Saven, J. G.; Therien, M. J. *Nano Lett.* **2009**, *9*, 1414.

(15) Nish, A.; Hwang, J.-Y.; Doig, J.; Nicholas, R. J. *Nature Nanotechnol.* **2007**, *2*, 640.

(16) Zou, J. H.; Liu, L. W.; Chen, H.; Khondaker, S. I.; McCullough, R. D.; Huo, Q.; Zhai, L. *Adv. Mater.* **2008**, *20*, 2055.

(17) Park, S.-J.; Kang, S.-G.; Fryd, M.; Saven, J. G.; Park, S.-J. *J. Am. Chem. Soc.* **2010**, *132*, 9931.

(18) Lipic, P. M.; Bates, F. S.; Hillmyer, M. A. *J. Am. Chem. Soc.* **1998**, *120*, 8963.

(19) O'Connell, M. J.; Bachilo, S. M.; Huffman, C. B.; Moore, V. C.; Strano, M. S.; Haroz, E. H.; Rialon, K. L.; Boul, P. J.; Noon, W. H.; Kittrell, C.; Ma, J. P.; Hauge, R. H.; Weisman, R. B.; Smalley, R. E. *Science* **2002**, *297*, 593.

(20) Lowe, A. B.; Sumerlin, B. S.; Donovan, M. S.; McCormick, C. L. *J. Am. Chem. Soc.* **2002**, *124*, 11562.

(21) Sill, K.; Emrick, T. *Chem. Mat.* **2004**, *16*, 1240.

(22) Zhu, M.-Q.; Wang, L.-Q.; Exarhos, G. J.; Li, A. D. Q. *J. Am. Chem. Soc.* **2004**, *126*, 2656.

(23) Mayya, K. S.; Schoeler, B.; Caruso, F. *Adv. Funct. Mater.* **2003**, *13*, 183.

Conclusion & Future Direction

In this thesis, I have described the relationship between materials properties and structures by using silica-based multicomponent nanoparticles and amphiphilic conjugated block copolymers. These studies demonstrated that the specific structures can be designed and synthesized to improve the materials properties and that the optical properties can be controlled by the self-assembled structures in a predetermined way.

In Part I, the synthesis of novel composite nanomaterials composed of fluorophore-labeled silica cores and hemispherical gold overlayers that are separated by spectroscopically inert silica spacers has been described. PL measurements at the single particle level demonstrated that the addition of the spacer layer effectively reduces the core PL quenching by the gold layer, rendering both constituents of the multicomponent nanostructures optically active. The versatility of this approach is further demonstrated by synthesizing analogous gold-coated nanoparticles based upon commercial fluorescent polymer nanoparticles. These multilayered nanoparticles were designed to combine the properties of fluorescent nanoparticles with the useful surface properties of gold, and such species could find utility in a wide range of biosensing applications. The hemispherical gold surfaces of these mutilayered particles can be readily functionalized with DNA and the DNA-modified hybrids recognize complementary DNA strands without the problem of nonspecific binding, showing promise for their use in DNA detection applications.

In Part II, hollow silica nanoparticles have been generated without a template based on the porous nature of silica and the high surface energy at the nanometer scale. Solid silica particles synthesized by the Stöber and microemulsion methods initially develop small pores inside the nanoparticles in slightly basic conditions due to base-catalyzed etching. With further reaction, those small seed pores merge into a single void to reduce the surface energy of small pores, generating well-defined hollow nanoparticles. This behavior is unique to nanometer-sized porous materials, and the shape evolution is size-dependent, reinforcing the importance of evaluating the reactivity and structural changes of nanomaterials as well as their physical properties at different size ranges. The mechanism described here can provide a simple way to generate uniform hollow nanoparticles of other porous materials such as tin oxide and titanium oxide.

In Part III, a novel class of amphiphilic conjugated block copolymers composed of Poly(3-octylthiophene) and poly(ethylene oxide) (POT-*b*-PEO) has been described. POT-*b*-PEO exhibits highly tunable photoluminescent colors spanning from blue to red and self-assembles into various supramolecular assemblies due to its amphiphilicity. The self-assembly structures can be readily controlled by altering the solvent composition or by other external stimuli. The color change was completely reversible demonstrating that the strategy can be used to manipulate light emission properties of conjugated polymers in a highly controllable manner without having to synthesize entirely new sets of molecules.

In Part IV, the as-synthesized POT-*b*-PEO was applied to produce the discreet polymer-nanomaterial hybrid structures. SWNTs are well dispersed in aqueous solution by using POT-*b*-PEO as a dispersant due to the strong π-π non-covalent interaction. POT-*b*-PEO acts as a structure-directing template as well as a component of multicomponent nanostructure and affects the geometrical development and particle conformation of gold and silver nanoparticles. This procedure should be applicable to many different types of metal nanoparticles and furthermore these hybrid particles are expected to find applications as a new class of materials of optoelectronic device and biological sensing.